

**AEDC-TR-06-17**



# **Hypersonic Wind Tunnel Nozzle Survivability for T&E Final Report: T&E/S&T Project**

**E. J. Felderman and D. T. Akers  
Aerospace Testing Alliance**

**and**

**C. T. Liu and J. Schneibel  
Oak Ridge National Laboratories**

**March 2007**

**Final Report for Period 1 Oct 2002 – 30 Sep 2006**

Approved for public release; distribution is unlimited.

**ARNOLD ENGINEERING DEVELOPMENT CENTER  
ARNOLD AIR FORCE BASE, TENNESSEE  
AIR FORCE MATERIEL COMMAND  
UNITED STATES AIR FORCE**

## NOTICES

When U. S. Government drawings, specifications, or other data are used for any purpose other than a definitely related Government procurement operation, the Government thereby incurs no responsibility nor any obligation whatsoever, and the fact that the Government may have formulated, furnished, or in any way supplied the said drawings, specifications, or other data, is not to be regarded by implication or otherwise, as in any manner licensing the holder or any other person or corporation, or conveying any rights or permission to manufacture, use or sell any patented invention that may in any way be related thereto.

References to named commercial products in this report are not to be considered in any sense as an endorsement of the product by the United States Air Force or the Government.

## DESTRUCTION NOTICE

For unclassified documents, destroy by any method that will prevent disclosure or reconstruction of the document.


## APPROVAL STATEMENT

This report has been reviewed and approved.



CHARLES R. VINING  
Applied Technology Division  
Test Operations Directorate

Approved for publication:  
For the Commander



JERE J. MATTY  
AEDC/XR Technical Director  
Test Operations Directorate

REPORT DOCUMENTATION PAGE					Form Approved OMB No. 0704-0188	
<p>The public reporting burden for this collection of information is estimated to average 1 hour per response, including the time for reviewing instructions, searching existing data sources, gathering and maintaining the data needed, and completing and reviewing the collection of information. Send comments regarding this burden estimate or any other aspect of this collection of information, including suggestions for reducing the burden, to Department of Defense, Washington Headquarters Services, Directorate for Information Operations and Reports (0704-0188), 1215 Jefferson Davis Highway, Suite 1204, Arlington, VA 22202-4302. Respondents should be aware that notwithstanding any other provision of law, no person shall be subject to any penalty for failing to comply with a collection of information if it does not display a currently valid OMB control number.</p> <p><b>PLEASE DO NOT RETURN YOUR FORM TO THE ABOVE ADDRESS</b></p>						
1. REPORT DATE (DD-MM-YYYY) 00-03-2007			2. REPORT TYPE Final Report		3. DATES COVERED (From – To) 1 Oct 2002 – 30 Sep 2006	
4. TITLE AND SUBTITLE  Hypersonic Wind Tunnel Nozzle Survivability for T&E Final Report: T&E/S&T Project					5a. CONTRACT NUMBER	
					5b. GRANT NUMBER	
					5c. PROGRAM ELEMENT NUMBER	
6. AUTHOR(S) E. J. Felderman and D. T. Akers Aerospace Testing Alliance  C.T. Liu and J. Schneibel, Oak Ridge National Laboratories					5d. PROJECT NUMBER 10054 and 10909	
					5e. TASK NUMBER	
					5f. WORK UNIT NUMBER	
7. PERFORMING ORGANIZATION NAME(S) AND ADDRESS(ES) Arnold Engineering Development Center/XRS Air Force Materiel Command Arnold AFB, TN 37389-9011					8. PERFORMING ORGANIZATION REPORT NO.  AEDC-TR-06-17	
9. SPONSORING/MONITORING AGENCY NAME(S) AND ADDRESS(ES) AEDC/XRS Arnold AFB, TN 37389					10. SPONSOR/MONITOR'S ACRONYM(S)	
					11. SPONSOR/MONITOR'S REPORT NUMBER(S)	
12. DISTRIBUTION/AVAILABILITY STATEMENT Approved for public release; distribution is unlimited.						
13. SUPPLEMENTARY NOTES Available in Defense Technical Information Center (DTIC).						
14. ABSTRACT  The nozzle in a hypersonic wind tunnel is generally subjected to a severe thermal environment. Several methods can be used to manage the energy absorbed by the nozzle, including backside cooling, film/transpiration cooling, and storing the energy in a heat-sink fashion. The development of new alloys that retain strength at higher temperatures has increased the feasibility of the self-limiting heat-sink mode of operation. This paper discusses the development of a series of such alloys as well as the applications for which they have been designed. The most promising of these is an Ir-Zr alloy. A nozzle has been fabricated from this alloy. Nozzle survivability tests with this alloy are planned.						
15. SUBJECT TERMS nozzle material, alloys, high-temperature material						
16. SECURITY CLASSIFICATION OF:			17. LIMITATION OF ABSTRACT	18. NUMBER OF PAGES	19a. NAME OF RESPONSIBLE PERSON	
a. REPORT	b. ABSTRACT	c. THIS PAGE			Jere J. Matty, AEDC/XR Technical Director	
Unclassified	Unclassified	Unclassified	Same as Report	51	19b. TELEPHONE NUMBER (Include area code) 931-454-6515	



## **PREFACE**

The work reported herein was conducted by the Arnold Engineering Development Center (AEDC), Air Force Materiel Command (AFMC), at the request of the Capabilities Integration Directorate, Technology Division (AEDC/XRS), for AEDC. The results of the technology development effort were obtained by the Aerospace Testing Alliance (ATA), the operations, maintenance, information management, and support contractor for AEDC, AFMC, Arnold Air Force Base, Tennessee, and by personnel of the Oak Ridge National Laboratories (ORNL), Oak Ridge, Tennessee, under Project Numbers 10054 and 10909. The ATA Project Managers were Dr. E. J. Felderman and Mr. P. A. Montgomery, and the AEDC Air Force Project Managers were Capt. Robert Wilson, Mr. S. A. Bancroft, and Mr. J. T. Staines. The data analysis was completed on 31 Aug 2006, and the manuscript was submitted for publication on 30 Sep 2006.

The authors would like to thank the Test Resource Management Center (TRMC) Test and Evaluation/Science and Technology (T&E/S&T) Program for their support. This work is funded through the Arnold Engineering Development Center, Arnold Air Force Base, TN.



## CONTENTS

	<u>Page</u>
ABSTRACT	
1.0 INTRODUCTION .....	3
2.0 HYPERSONIC SIMULATION REQUIREMENTS.....	3
3.0 NOZZLE REQUIREMENTS FOR DIFFERENT TYPES OF HYPERSONIC FACILITIES.....	4
3.1 Nozzle Issues/Strategies.....	5
3.2 Temperature History Examples .....	6
4.0 NOZZLE MATERIALS DEVELOPMENT.....	13
4.1 Iridium Alloy Development.....	14
4.2 MoSiB Alloy Development .....	32
4.3 MoReX Alloy Development.....	38
4.4 Ni-Coated Cu - Back-Side-Cooled Arc-Heater Nozzles .....	45
5.0 SUMMARY/CONCLUSIONS.....	48
6.0 REFERENCES .....	49

## ILLUSTRATIONS

<u>Figure</u>	<u>Page</u>
1. System/Facility Performance for Flight Duplication.....	4
2. Predictions of Nozzle Throat Heat-Transfer Coefficients.....	5
3. Temperature Profile in Nozzle Throat, AEDC FPST .....	7
4. Temperature-Time History in a Tunnel 9, Mach 14 Nozzle Throat Insert, Po = 22,000 psia, To = 2800°F, Run Time = 1 s .....	8
5. Radiantly Driven Hypersonic Wind Tunnel (RDHWT) Process Path.....	8
6. Recovery Temperature Through a Typical RDHWT Nozzle .....	9
7. Approximate Strength Requirements for the RDHWT Nozzle Throat Area for Design and Off-Design Points.....	10
8. RDHWT Nozzle Throat Insert Subjected to a 1-s Heating Pulse.....	11
9. Temperature-Time Histories in an Iridium Nozzle Insert with Steel Backing .....	12
10. Heat Penetration into Nozzle Throat Insert .....	12
11. Temperature Profiles Through a Backside-Cooled Copper Nozzle .....	13
12. Microstructural Features of the 4.5-Percent Zr Alloy Showing Fine Dendritic Structures with Dark Regions, Fine and Stable Eutectic Structures, Containing a Mixture of Ir and Ir <sub>3</sub> Zr Phases.....	15
13. Yield Strength and Temperature Comparison of IRT-12 and Haynes-25 Alloys .....	16
14. Results of Oxidation Test of Iridium Alloy .....	17
15. Sketch of Nozzle .....	19
16. FEA Thermal Model.....	19
17. Plot of Temperature vs. Time at the Throat Axial Location.....	21
18. Assembly Temperature Distribution at 0.09 s .....	22

19. Assembly Temperature Distribution at 1 s .....	22
20. Assembly Temperature Distribution at 5 s .....	22
21. Confirmed Thermal Distribution at 0.09 s .....	23
22. Pressure-Loaded Stress Model.....	23
23. Equivalent Stress Compared to Yield Strength .....	24
24. Stress Intensity .....	25
25. Principal Stress Distribution for Direction 1 .....	26
26. Principal Stress Distribution for Direction 2 .....	27
27. Principal Stress Distribution for Direction 3. ....	28
28. Schematic of Drip-Casting Technique.....	30
29. Vacuum Arc Remelting Process Used to Produce Alloy Ingot .....	30
30. Iridium Alloy Nozzle for Testing in the A2-Lite.....	31
31. Schematic of A2Lite .....	31
32. Schematic Section of Mo-Si-B Phase Diagram at 1600°C.....	32
33. Scanning Electron Micrograph of Mo-10Si-14B Microstructure at. % Specimen after Casting and Annealing (1 day/1600°C/Vacuum) .....	33
34. Optical Micrograph of a Transverse Section of Vacuum-Annealed and Hot-Pressed Mo-16.8Si-8.4B (at. %) Powder .....	35
35. Room-Temperature Tensile Test of Mo-26 at. % Re (Test N026-T2) .....	40
36. Stress-Strain Curve for Compression of Mo-26Re-0.05Zr (at. %) at 1427°C and $10^{-3} \text{ s}^{-1}$ .....	41
37. Oxygen-Containing Nodules on a Room-Temperature Fracture Surface of Mo-26 at. % Re .....	43
38. Room-Temperature Fracture Surface of Mo-26Re-0.1Zr (at. %).....	44
39. Room-Temperature Fracture Surface of Mo-26.7Re-7.6Cr-0.1Zr (at. %) .....	44
40. Optical Micrograph of Cross Section Through Electroplated Amzirc Material.....	47
41. SEM Micrograph of Room Temperature Fracture Surface of As-Plated Amzirc .....	47
42. SEM of Fracture Surface of Ni-Plated and Annealed Amzirc Sheet.....	48

## TABLES

<u>Table</u>	<u>Page</u>
1. Weight Changes for Candidate Alloys .....	17
2. Thermal Properties.....	18
3. Material Properties Used in FEA Thermal Model Analysis.....	20
4. Specimens Subjected to Thermal Shock Tests (Quenching from 1700 K into Water) .....	36
5. Vickers Hardness (1000 g/ 15-s dwell time) of Mo-Re Alloys .....	38
6. Room-Temperature Tensile Test Data for Mo-26Re (at. %) Alloys. ....	40
7. 0.2% Yield Stress Values at 1427°C and a Strain Rate of $10^{-3} \text{ s}^{-1}$ .....	42
8. Carbon and Oxygen Concentrations in Mo-26 at. % Re (Specimen N026) .....	42
9. Results of Room-Temperature Compression Tests .....	43
10. Strength of Hot-Rolled Inconel 600 (Ni-16Cr-6Fe, wt %).....	45
11. Physical Properties of Inconel 600 .....	45
12. Thermal Expansion of Copper and Nickel, Percent.....	45



## 1.0 INTRODUCTION

Hypersonic wind tunnels will be required for the development of future hypersonic flight weapons systems. The types of hypersonic systems envisioned are offensive and defensive missiles, aircraft, and space transportation systems. The classes of ground testing include propulsion (both air-breathing and rocket); aerodynamic force, moment, and control; aero-thermal structural; aero-optic sensor; and impact testing. Most systems require facilities for performance, operability, and durability validation testing. Operability and durability testing require test times on the order of seconds to minutes. The required velocity, gas density, and test time requirements often exceed any existing test capability and test technology.

Hypersonic wind tunnels typically use converging-diverging nozzles to expand the flow to the desired Mach number and velocity. The test gas must be heated to the needed stagnation temperatures before expansion through the nozzle to prevent gas condensation and to duplicate hypersonic velocities of flight. These temperatures can range up to several thousand degrees Kelvin, depending upon the desired test conditions. In addition, the test gas generally must be pressurized up to several thousand atmospheres to achieve the required density of flight and dynamic pressure. This combination of very high temperature and pressure means that the heat and mechanical loading to the nozzle, especially near and at the nozzle throat, can greatly exceed the temperature and structural loading capability of existing high-temperature and high-strength materials for nozzles.

An alternative approach to hypersonic wind tunnel design being pursued is called the Radiatively Driven Hypersonic Wind Tunnel (RDHWT, Ref. 1). In this approach, the test gas is contained in the reservoir at ultra-high pressure but at modest temperature (750 K). Energy is subsequently added in the supersonic portion of the nozzle in order to achieve the enthalpy level required for the test condition. Keeping the stagnation temperature at a relatively low level (750 K) makes it much easier to design the ultra-high pressure reservoir. However, some of the enthalpy stored as pressure in the reservoir manifests itself as temperature as the pressure drops in the nozzle; hence, the recovery temperature at the throat may reach 1700 K. (Refs. 2 and 3) While this recovery temperature is less than that experienced in many conventional facilities, the pressure is still high, and thus the nozzle throat heat loads are quite challenging. Nevertheless, the relatively modest recovery temperature of 1700 K suggests the possibility of developing a material that will retain sufficient strength at 1700 K to contain the pressure. The nozzle could then operate in the self-limiting heat-sink mode (described in more detail in subsequent sections of this report). This report documents the effort to develop one or more materials suitable for this application.

## 2.0 HYPERSONIC SIMULATION REQUIREMENTS

The simulation capabilities of various hypersonic test facilities are summarized in Fig 1. Hypersonic flight simulations usually match either the Mach number or the velocity (enthalpy), but seldom both at the same time. Some applications (such as scramjet engine testing and durability testing) require simultaneous Mach number and enthalpy matching; this is usually referred to as “flight duplication.” The limits shown in

Fig. 1 for each facility represent flight duplication. Conventional facilities can handle simulations up to Mach 8 or slightly higher, using combustion heating. Impulse tunnels (free-piston shock tubes) can cover the Mach 8 to 15 range with millisecond test times, sufficient for performance testing only. The proposed RDHWT (Refs. 1 through 3) is being developed to cover the Mach 8 to 12 or 8 to 15 range with test times on the order of seconds. The design goal of the RDHWT is to achieve Mach 12 flight conditions at a dynamic pressure of  $q = 2000$  psf using clean air. This corresponds to the lower edge of the scramjet corridor at Mach 12, as shown in Fig 1; consequently, the entire airbreathing flight corridor could be duplicated from Mach 8 to 12 or 15.

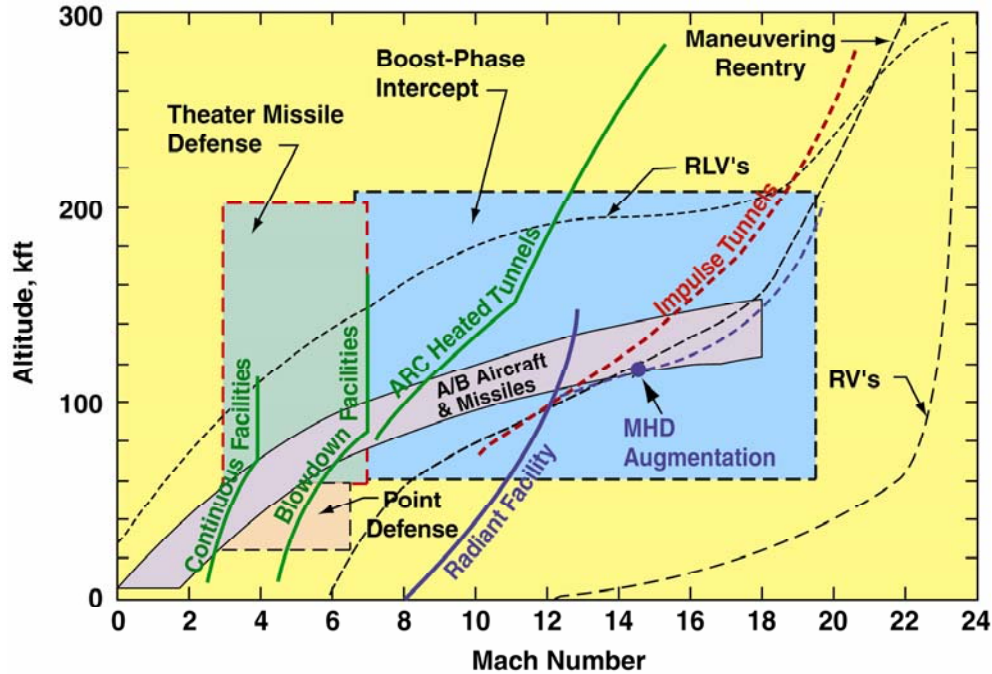


**Figure 1. System/Facility Performance for Flight Duplication**

### **3.0 NOZZLE REQUIREMENTS FOR DIFFERENT TYPES OF HYPERSONIC FACILITIES**

Heat-sink nozzles are suited for hypersonic test facilities with test times of several seconds or less. These facilities include the free-piston shock tube (FPST), blowdown tunnels, and the proposed RDHWT concept. Predicted heat-transfer coefficients for these types of facilities are shown in Fig. 2 using a correlation developed in Ref 4. The design heat-transfer coefficients for the FPST and the RDHWT are seen to be quite high. The heat-transfer coefficients for the Tunnel 9 configurations and the current operating condition for the FPST are lower, but still quite challenging. In contrast, active-cooled nozzles are required for facilities with longer run times such as arc-heated or combustion-driven facilities (e.g., the AEDC APTU facility). These facilities generally depend on backside water cooling, film cooling, or transpiration cooling (film and transpiration cooling are not treated in detail here). However, the heat-transfer coefficients for an arc-heated and a combustion-driven facility are also shown in Fig. 2. These conditions can be handled with backside water cooling, but such conditions approach the limits of this technique, (Ref. 5).

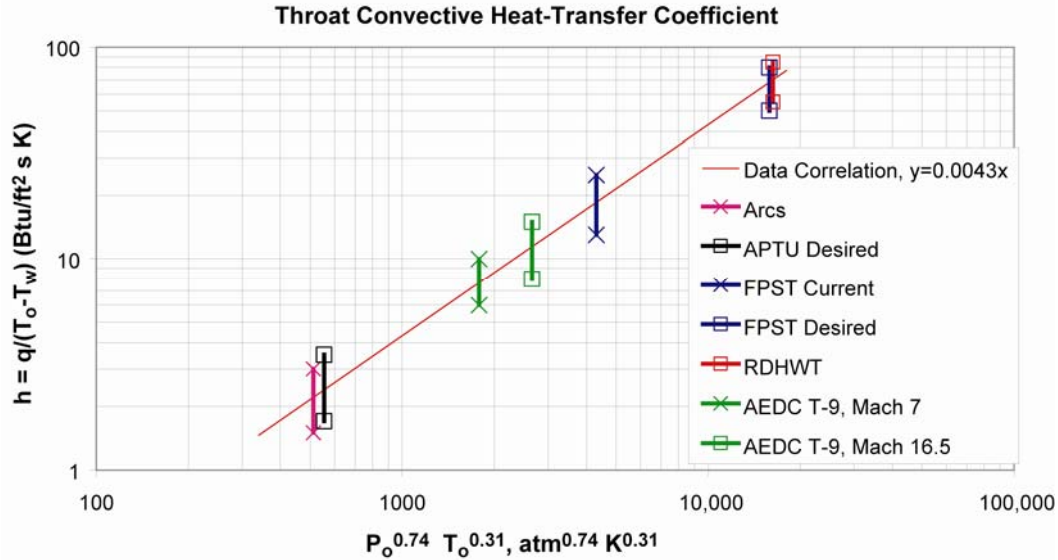


**Figure 2. Predictions of Nozzle Throat Heat-Transfer Coefficients**

### 3.1 Nozzle Issues/Strategies

Depending on the type of facility, various approaches can be used to manage the heat loading at the nozzle throat. The throat protection schemes that have been used include:

- heat sink – limited time
- heat sink – self-limiting
- backside cooling
- film or transpiration cooling

The heat-sink method attempts to store the heat transferred to the nozzle mass. This method is especially suited to short-run-time facilities since there is a limit to the amount of energy that can be stored. The important material properties are a high thermal capacity and a high thermal conductivity. A high thermal conductivity is important in order to transfer energy into the metal so that the metal temperature at the gas interface does not exceed the melting temperature or such temperature level that the required strength drops below the imposed stress level. If the recovery temperature is such that a material can be developed that will maintain strength at that temperature, then the heat transfer becomes “self-limiting.” The heat transfer at the nozzle throat may be expressed as:

$$Q = h(T_r - T_w)$$

The heat-transfer rate,  $Q$ , is expressed as the product of a heat-transfer coefficient,  $h$ , and the driving potential,  $(T_r - T_w)$ , where  $T_r$  is the recovery temperature and  $T_w$  is the wall temperature (material temperature at the gas interface). If a material can be found to retain sufficient strength as  $T_w \rightarrow T_r$ , then the heat transfer can be limited since  $Q \rightarrow 0$  as  $T_w \rightarrow T_r$ . Candidates for this operational mode are hypersonic facilities that have a moderate recovery temperature,  $T_r$ , such as the RDHWT. A potential concern with this approach is that the heat will eventually soak into the nozzle insert support material and exceed its strength capability.

If the recovery temperature exceeds the melting temperature of the nozzle material and the run time is long, then it may be necessary to backside cool the nozzle in order to keep the nozzle temperature within reasonable bounds.

## **3.2 Temperature History Examples**

### **3.2.1 AEDC Free-Piston Shock Tube**

The AEDC free-piston shock tube (FPST) experiences high stagnation pressures and temperatures, and hence large nozzle throat heat fluxes. Stagnation temperatures may be as high as 10,000 K. The design stagnation pressure is 10,000 atm, but the current operating limit is some 2000 atm. The nozzle is in fact the limiting component. Nozzle material surface temperatures quickly rise to levels where the yield strength is degraded and melting can occur. Predicted material temperatures for typical conditions in the AEDC FPST are shown in Fig. 3. In order to provide perspective, the x-axis in Fig. 3 spans the distance from the flow centerline to the outside of the nozzle insert. Note that the heating is very localized at the gas-metal interface.

It is also noted that the material temperature rises to very high levels in a very thin layer near the gas interface. This layer is shown expanded in Fig. 3 (b). Yielding occurs in compression during heating. This thin layer is then placed in tension as cooling occurs, with subsequent cracking occurring as the yield point is exceeded.

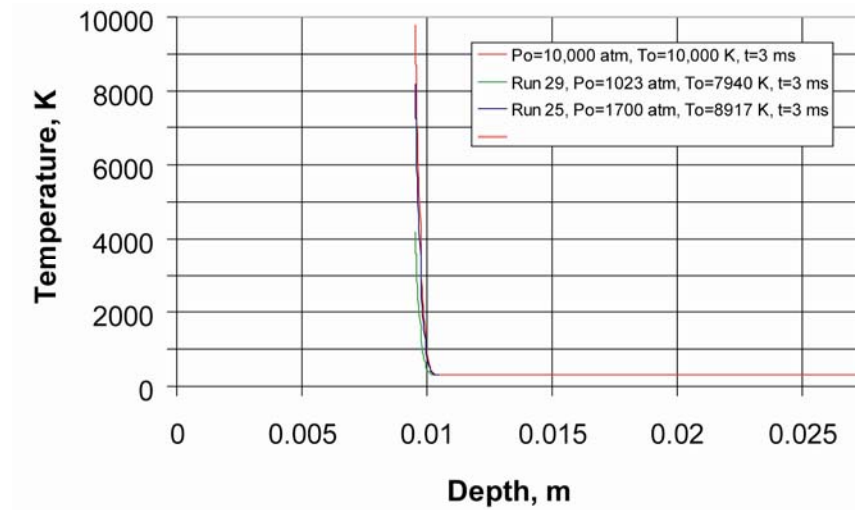
### **3.2.2 AEDC Tunnel 9**

The Tunnel 9 stagnation conditions are less severe than those for the shock tube. The material temperature histories are shown in Fig. 4 for a 1-s run with the Mach 14 nozzle. The heat penetration is deeper, and the surface temperature rises less, all over a much longer time span than experienced in the FPST. The nozzle throat insert material, Columbium, C103, will be weakened sufficiently at the temperatures shown to experience yielding. The surface temperature does not quite reach a level close enough to the stagnation temperature in one second to be considered in the “self-limiting” mode, but it is close to that mode.

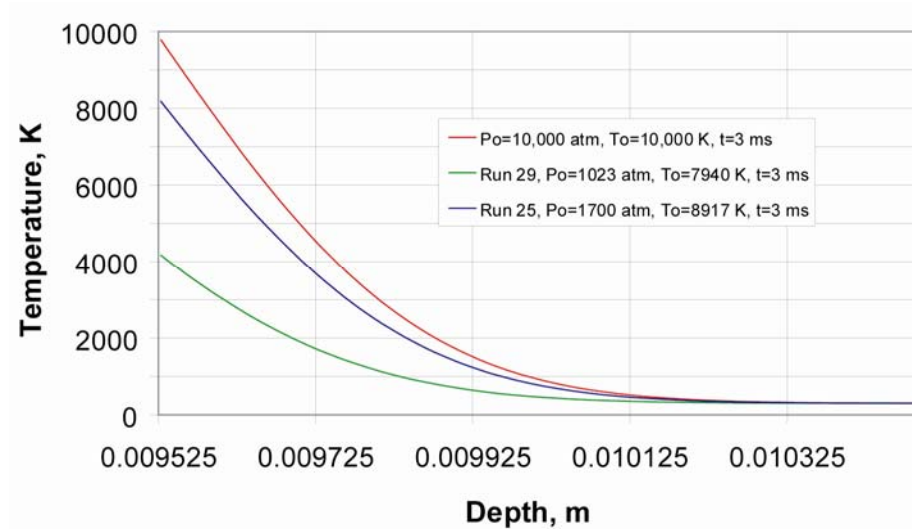
### **3.2.3 Radiatively Driven Hypersonic Wind Tunnel**

With the RDHWT concept, the test gas is contained in a reservoir at ultra-high pressure (2300 MPa), but at a modest temperature (750 K), which makes it much easier to design the ultra-high pressure reservoir (Ref. 2). Energy is subsequently added in the supersonic portion of the nozzle in order to achieve the enthalpy necessary to simulate the desired test condition. This process is depicted in an H-S diagram in Fig. 5.

Conventional wind tunnels usually function on the right side of the H-S diagram where  $H = H(T)$ . Material strength limits how high one can go in reservoir enthalpy; consequently, when expanded to a high Mach number, the static temperature is often too low. The RDHWT starts in the reservoir on the left side of the H-S diagram where  $H = H(P, T)$ , where significant energy (enthalpy) can be stored as pressure. One then expands through the throat and more energy is added, followed by further expansion to Mach



**a. Flow Centerline Through Nozzle Insert**



**b. Gas-Metal Interface, Expanded View**

**Figure 3. Temperature Profile in Nozzle Throat, AEDC FPST**

12 conditions, perhaps with MHD acceleration to Mach 15. The nozzle throat of the RDHWT is not subjected to as high a temperature as would exist in a conventional wind tunnel; nevertheless, it is exposed to a challenging environment. As the test gas expands from the reservoir, the pressure drops from 2300 MPa to approximately 600 MPa at the throat. Since considerable enthalpy is stored as pressure in the reservoir, as the pressure drops, the enthalpy manifests itself as temperature; hence, the recovery temperature at the throat may reach 1700 K<sup>3</sup>, as depicted in Fig. 6.

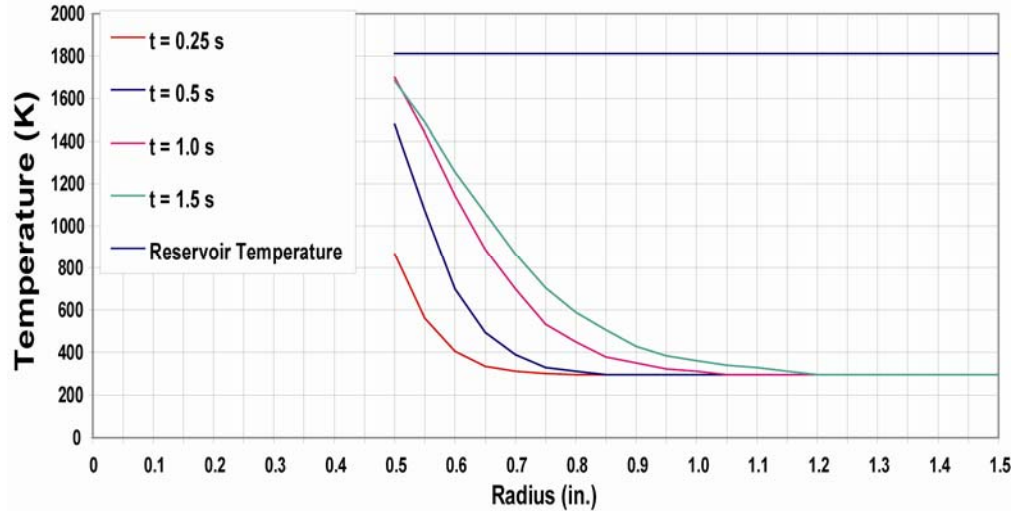


**Figure 4. Temperature-Time History in a Tunnel 9, Mach 14 Nozzle Throat**  
**Insert,  $P_o = 22,000$  psia,  $T_o = 2800^\circ\text{F}$ , Run time = 1 s**

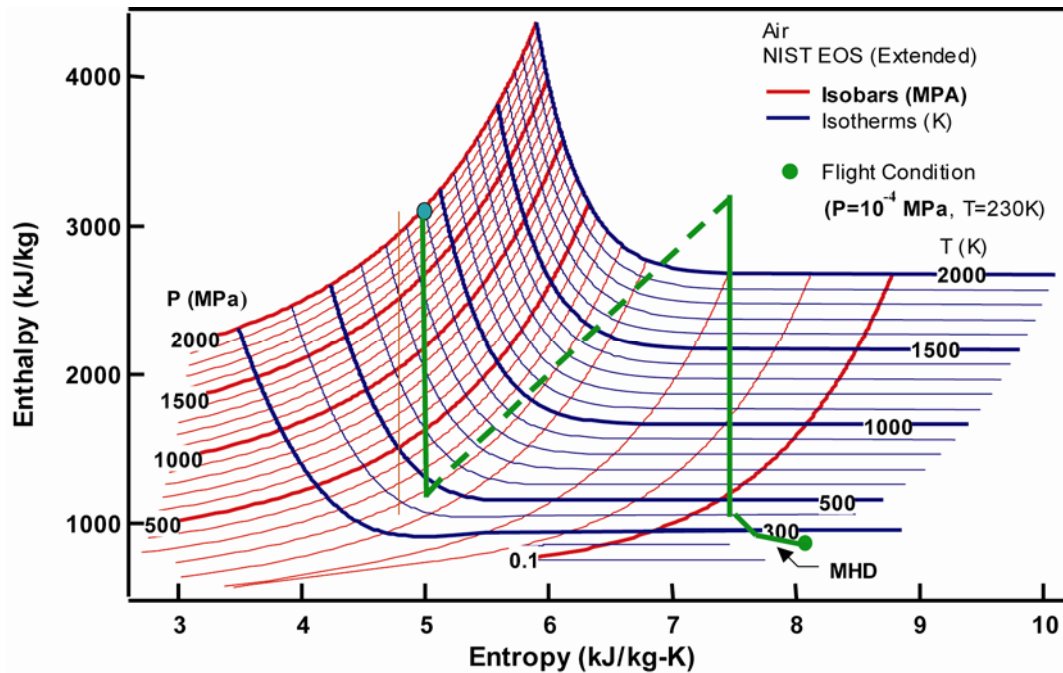


**Figure 5. Radiantly Driven Hypersonic Wind Tunnel (RDHWT) Process Path**

The shaded area in Fig. 6 is composed of many streamlines. The centerline streamline (at the bottom of the picture) shows the static temperature dropping during the expansion (i.e., following conventional wisdom). However, in the boundary layer, near the wall (at the top of the picture) as the flow slows and some of the kinetic energy is “recovered,” this energy must manifest itself as temperature because the pressure has dropped during the expansion. (Since the recovery process in the boundary layer is not isentropic, the process involves moving to the right on the H-S diagram where the pressure dependence [ $H = H(P,T)$ ] is weakening.)

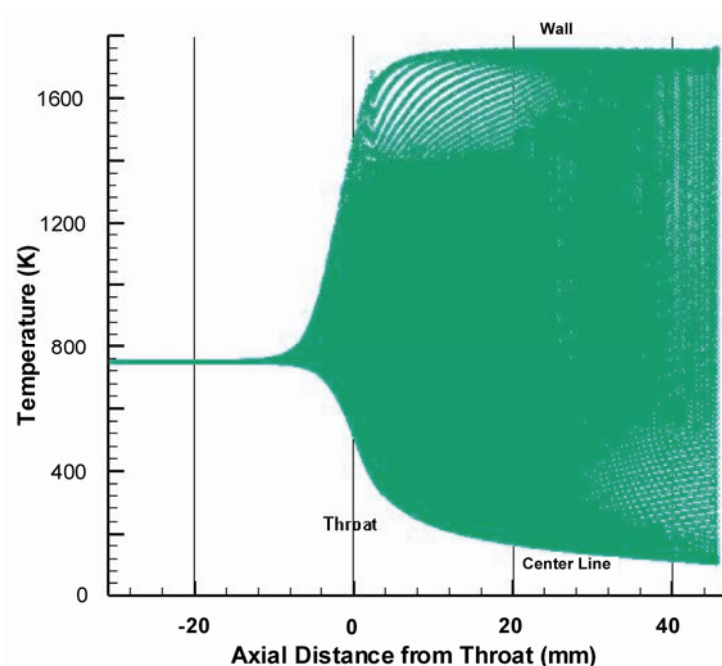


**Figure 6. Recovery Temperature Through a Typical RDHWT Nozzle**

### 3.2.3.1 RDHWT Requirements

The three major requirements for the RDHWT nozzle throat are:

- a) Heat load management
- b) Oxidation resistance
- c) Erosion resistance

Expanding from a potential maximum reservoir pressure of 2300 MPa, the throat pressure will be in the 500- to 600-MPa range. This pressure is much higher than normally experienced at the throat in a conventional hypersonic wind tunnel; therefore, the heat-transfer coefficient will be unusually large. The recovery temperature will depend on the test conditions but at the design point of Mach 12 at  $q = 2000$  psf it is nearly 1700 K.<sup>3</sup> Off-design operating points fall at smaller values of the recovery temperature and hoop stress (lower pressure), as shown in Fig. 7. Because of the large heat-transfer coefficient, the driving potential ( $T_r - T_w$ ) will have to be reduced to a very small number before  $Q$  becomes small. In other words, the throat material will have to function at the recovery temperature,  $T_r$ .

As a first approximation, the throat area of the nozzle can be treated as a thick-walled pressure vessel. The hoop stress in the nozzle throat area then is approximately equal to the static pressure at that location. The design point of Mach 12 at  $q = 2000$  psf implies a strength requirement of 600 MPa at 1700 K (see Fig. 7). Lowering either the Mach number or the dynamic pressure reduces the severity of the nozzle throat environment. (The severity of the throat environment is reduced in two ways, by reducing the strength requirement and by reducing the operating temperature.)



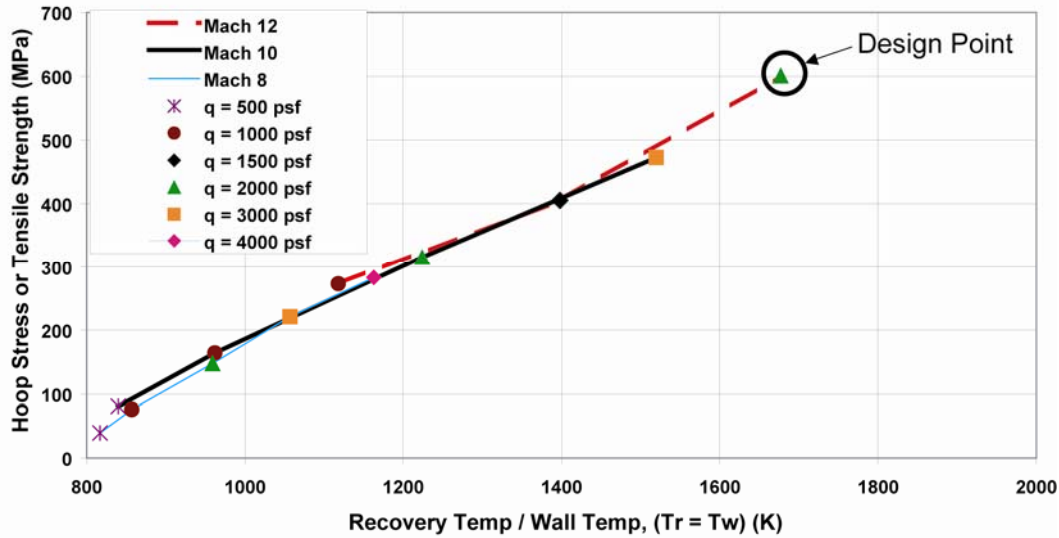


**Figure 7. Approximate Strength Requirements for the RDHWT Nozzle Throat Area for Design and Off-Design Points**

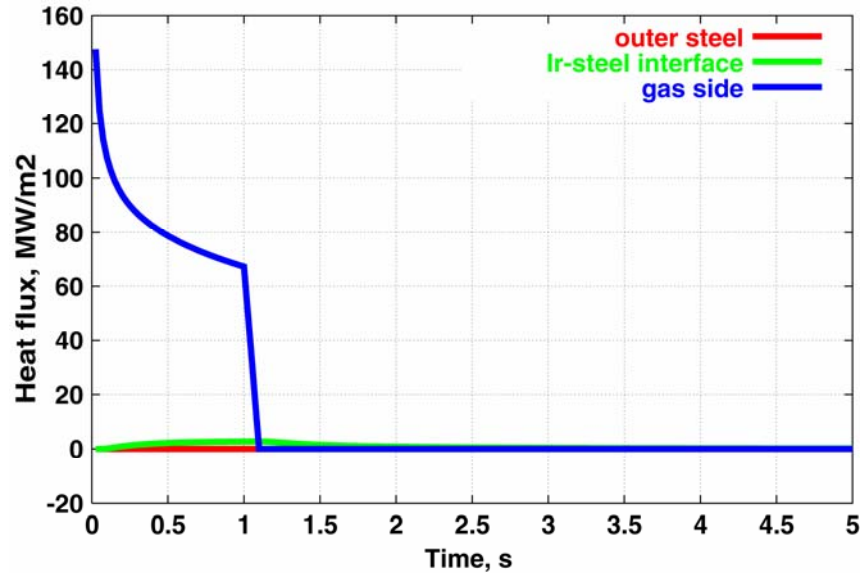
### 3.2.3.2 Nozzle Thermal Behavior.

Typical predicted thermal behavior for an A2Lite nozzle throat insert is shown in Fig. 8 for a run time of one second. The A2Lite is a proof-of-concept device designed to show ultra-high pressure system feasibility and to test nozzles for the RDHWT concept. The nozzle is composed of an inner Iridium nozzle contour wrapped in an outer steel jacket. It can be seen from Fig. 8a that the heat flux starts very high and drops quickly (Fig. 8b), becoming “self-limiting” as the surface temperature climbs quickly to approach the recovery temperature of 1634 K. Heat continues to penetrate the throat insert until the run ends at one second, by which time the Iridium-steel interface temperature has risen some 200 K. This is cause for concern if the initial temperature is equal to the reservoir stagnation temperature of 750 K, but it probably can be tolerated. After the run ends at one second, the heat is dissipated into the steel surrounding the Iridium nozzle insert.

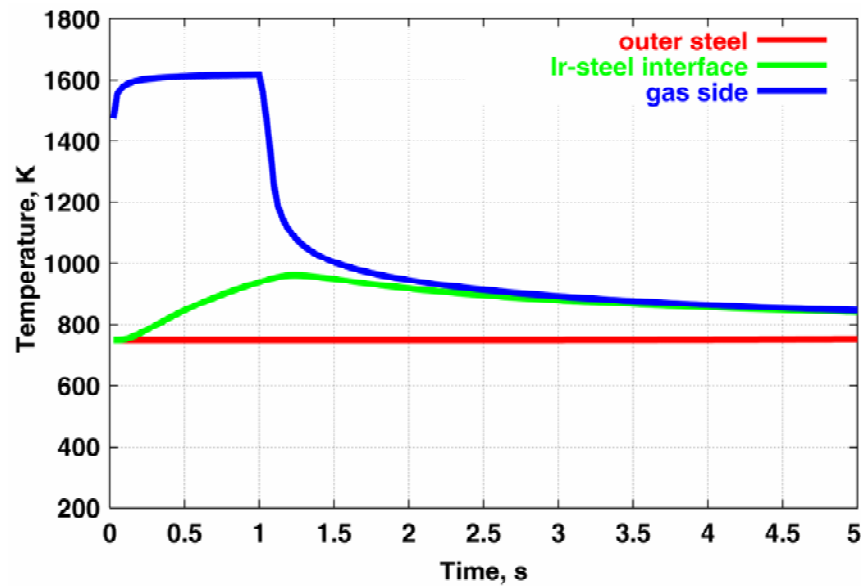
For runs longer than one second, the heat will continue to penetrate, raising the steel temperature to a higher level. As shown in Fig. 9a, where the nozzle is assumed to be initially at 750 K, the Ir-steel interface reaches 1178 K after five seconds, a temperature sufficient to compromise the strength of the steel. If the nozzle is initially at 300 K, as is shown in Fig. 9b, the temperature at the Ir-steel interface is 945 K, which is tolerable. However, keeping the nozzle at 300 K prior to the run may be problematic. Thermal shock considerations may dictate that the nozzle be heated to some temperature closer to the recovery temperature before the run is initiated.

The heat penetration is shown in a slightly different way in Fig. 10, where isotherms, throughout the nozzle insert and surround, are shown at one-second intervals.





a. Predicted Heat Flux

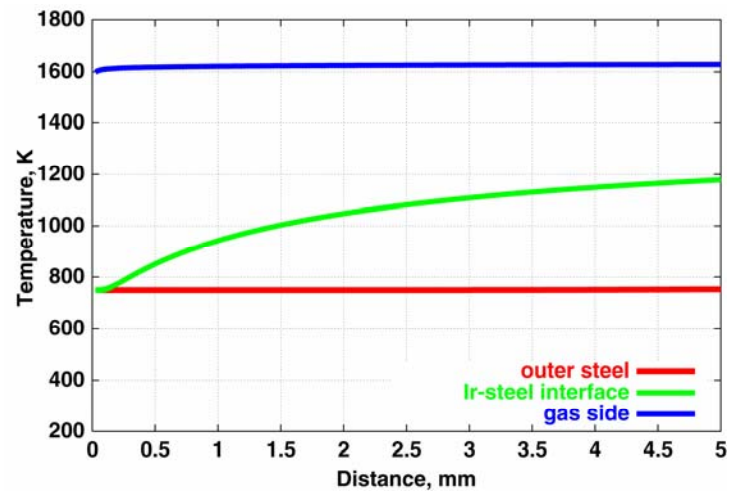


b. Predicted Temperature-Time Profiles

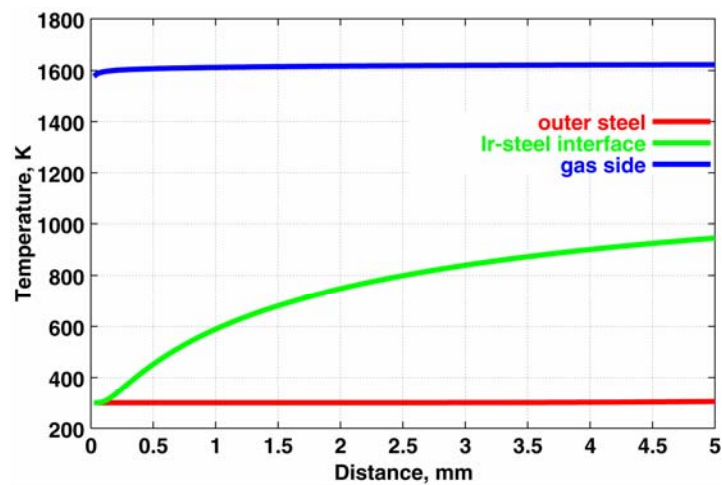
**Figure 8. RDHWT Nozzle Throat Insert Subjected to a One-Second Heating Pulse.**

### 3.2.4 Backside-Cooled Nozzles

When the gas recovery temperatures are high compared to the nozzle material melting temperature and run times are long, it is necessary to actively cool the backside of the nozzle in order to retain adequate strength and prevent melting. Predicted temperatures in a copper nozzle wall are shown in Fig. 11. The effects of coatings are also shown. The coating allows the gas-coating interface temperature to go significantly higher, while the copper can be maintained at a somewhat lower temperature. To be effective, the coating must have a lower thermal conductivity than the copper and be able



(a) Initial Temperature = 750 K



(b) Initial Temperature = 300 K

Figure 9. Temperature-time histories in an Iridium nozzle insert with steel backing.

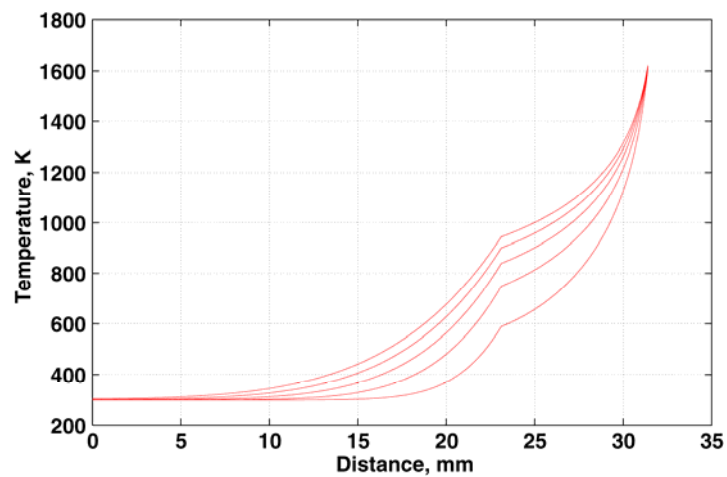
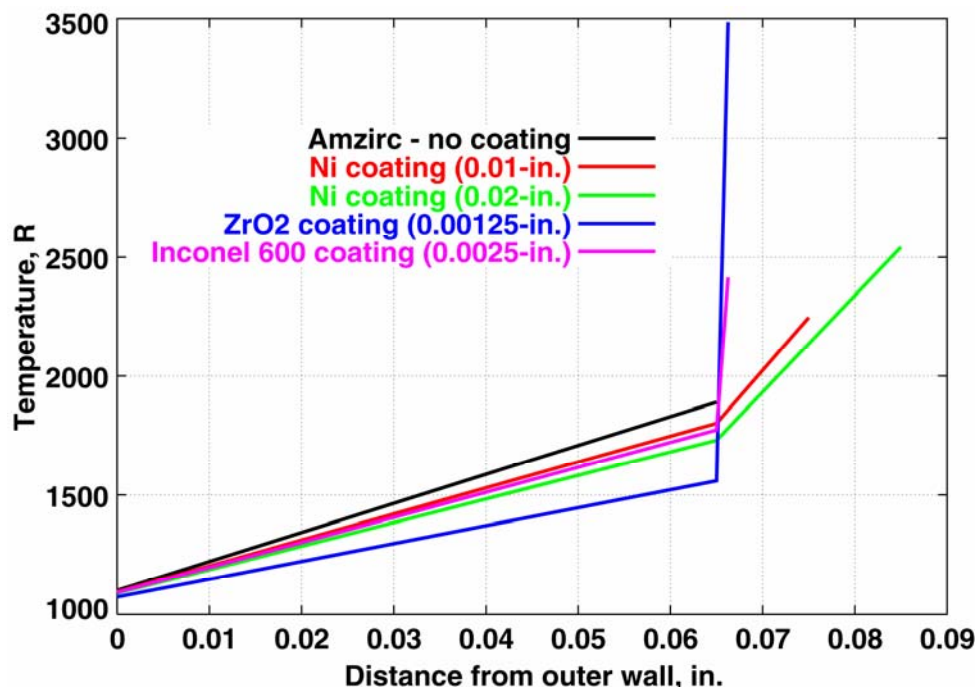


Figure 10. Heat Penetration into Nozzle Throat Insert



**Figure 11. Temperature Profiles through a Backside-Cooled Copper Nozzle**

to withstand a higher temperature. A ceramic coating (such as  $\text{ZrO}_2$ ) is potentially the most effective, but maintaining a bond at the interface that will resist spalling under thermal shock has always been a problem. Work with a Ni coating is reported in a following section.

#### 4.0 NOZZLE MATERIALS DEVELOPMENT

High-temperature alloys are needed for a number of different applications. In addition to the application addressed here (nozzles for hypersonic facilities), the thermal efficiency of heat engines and energy conversion devices could be increased through increased operating temperature. The operating temperature of advanced energy conversion systems is currently limited by structural materials that lose their strength and oxidation resistance at high temperatures. Ni-based superalloys can be used at temperatures up to  $950^\circ\text{C}$  in polycrystalline forms and at temperatures up to  $1100^\circ\text{C}$  in single crystalline forms. Structural ceramics, on the other hand, possess adequate strength at higher temperatures, but their poor fracture toughness and environmental sensitivity greatly restrict their use as engineering materials. At the beginning of this investigation, there were literally no alloys that could be used as structural materials at temperatures above  $1200^\circ\text{C}$  in oxidizing environments.

A number of alloys were considered including MoRe alloys, MoSiB alloys, and Iridium alloys (Refs. 6 through 8). An Iridium-based alloy system is an attractive candidate because of its proven oxidation resistance. The strength of unalloyed Iridium at elevated temperature (e.g.,  $1700\text{ K}$ ) is not impressive, but at the beginning of this investigation there was good potential for improving its strength with proper alloying.

If thermal loading is managed through the “self-limiting” heat-sink approach (Ref. 6), then nozzle materials for RDHWT hypersonic wind tunnel nozzle throats are required to withstand exposure to high-pressure oxidizing gases at temperatures up to 1700 K. Because of the high-temperature requirement, only ceramic materials and refractory metal alloys can be considered for such applications. Ceramic materials have good strength at high temperatures but poor fracture toughness and limited thermal shock resistance at ambient temperatures. Refractory metal alloys, such as Nb and Ta-based alloys, on the other hand, have high melting points and good toughness but poor oxidation resistance at elevated temperatures. Refractory noble-metal alloys based on Ir are of interest for high-temperature use because of their high melting point (~2440°C) and good oxidation resistance in air.

#### 4.1 IRIDIUM ALLOY DEVELOPMENT

Existing Ir-based alloys had only limited strength at temperatures above 1200°C; as a result, this alloy development effort has been devoted to the improvement of the strength of Ir-based alloys by both solid solution hardening and particle strengthening through alloy additions. During the development, it must be ensured that strength improvement is not achieved at the expense of oxidation resistance and the high melting point of Ir alloys.

An Ir-based alloy, Ir-0.3W doped with 60-wppm Th, was selected as the base composition for alloy development. This alloy has good ductility at ambient temperatures but limited strength at elevated temperatures. For instance, this alloy has a yield strength of only 52 MPa at 1370°C. Various elements were considered as candidates for alloy additions; their attributes and shortcomings are discussed below.

Nb effects First, alloy additions of Nb with or without additional Zr were made to the base composition. All alloys were prepared by arc melting and drop casting into a Cu mold. The hardness of these alloys was determined in both the as-cast condition and in an annealed condition (1 h at 1500°C in vacuum). Additions of Nb are very effective in hardening the Ir-based alloy, with the hardness increasing from 280 to 928 DPH at 10 percent Nb. Metallographic examination shows a two-phase structure in the Nb-containing alloys. However, the Nb additions apparently cause microcracking along grain boundaries. Microalloying additions of carbon and boron were made to Nb-containing alloys for refining grain size in as-cast ingots. These elements were found to reduce the microcracking tendency somewhat, but they could not eliminate it.

Ta effects Although Nb is effective in hardening, it tends to crack grain boundaries. As a result, it was necessary to search for other alloying elements for strengthening. It was found that 10 percent Ta added to the Ir base composition was a good strengthener, but it also caused severe grain-boundary cracking, just as Nb additions did. Thus Ta cannot be used as an alloying element for strengthening of Ir alloys.

Zr effects Zr was selected as an alloying addition to the Ir base composition. Samples containing 0.7 to 5.0 at. % Zr were prepared successfully by arc melting and drop casting. Zr is also an effective hardener, just like Nb and Ta additions. It is

important to point out that Zr additions do not induce grain-boundary cracks in cast alloys. This is indicated in Fig. 12, which shows fine dendritic microstructures with no grain-boundary cracks at all. The dark regions are eutectic structures containing a mixture of Ir and  $\text{Ir}_3\text{Zr}$  phases. These fine eutectic structures are expected to harden Ir-based alloys at ambient and elevated temperatures.

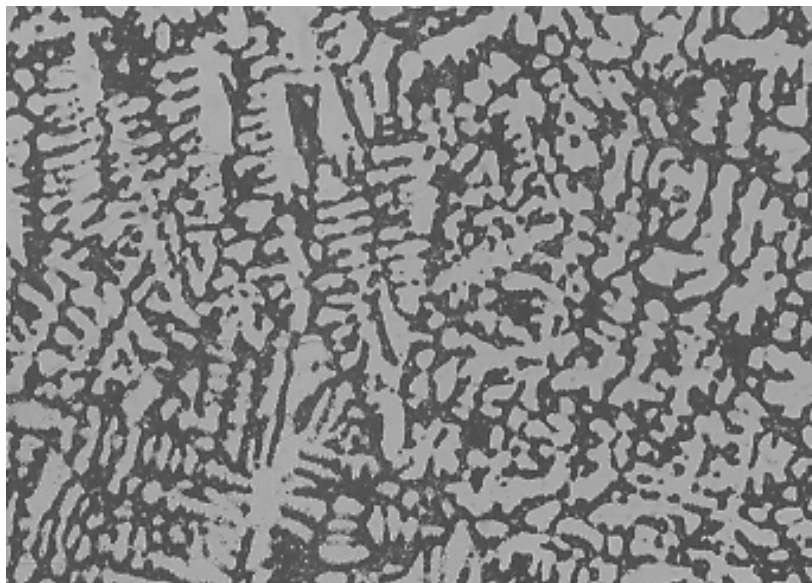


**Figure 12. Microstructural Features of the 4.5-percent Zr Alloy Showing Fine Dendritic Structures with Dark Regions, Fine and Stable Eutectic Structures Containing a Mixture of Ir and  $\text{Ir}_3\text{Zr}$  Phases**

Hf effects Hf, chemically similar to Zr, was also added to the Ir-base composition. Hf and Zr additions produce similar microstructures in the Ir-base alloys. Both alloys exhibited fine dendritic structures with eutectic structures in the dark regions. Hf is also an effective hardener in the Ir-based alloys. The composition of second-phase particles observed was analyzed using an electron microprobe at the Oak Ridge National Laboratories (ORNL). The particles contained roughly 18.5 at. % Hf (possibly  $\text{Ir}_3\text{Hf}$  phase), with the balance being Ir.

A system consisting of Iridium alloyed with Zr was eventually selected for final optimization. A total of 12 alloys were prepared and characterized. An optimum composition of [Ir -4.5Zr -0.3W -0.31C -0.005Th (at. %)] was selected.

#### **4.1.1 Strength Considerations**

Initial characterization of the various candidate materials was done by using hardness testing. More detailed characterization was accomplished with compression testing. Increasing the amount of alloying generally increases both hardness and strength. However, at some point, the increased hardness/strength comes at the expense of decreasing ductility and increasingly brittle characteristics. Therefore, a compromise in composition must be sought.

The mechanical properties of Iridium high-temperature (IRHT or IRT) alloys were initially determined by compression testing at room temperature and at 1427°C (1700 K). Rod specimens 2.5 mm in diameter by 5 mm long were prepared by electro-discharge machining (EDM), followed by annealing for one hour at 1500°C. The room-temperature tests were conducted on an MTS testing machine with a 50,000-lb load cell, and the elevated temperature tests were performed on an Instron testing machine with a 1,000-lb load cell. Test results were obtained at a strain rate of  $2 \times 10^{-2}$  per second.

The strengths of the IRT-12 alloy at ambient and elevated temperatures are shown in Fig. 13. The Iridium alloy is seen to maintain a strength of 700 MPa at 1700 K, as required for the RDHWT nozzle throat application. By comparison, the Haynes 25 alloy has lost essentially all of its strength at 1700 K.

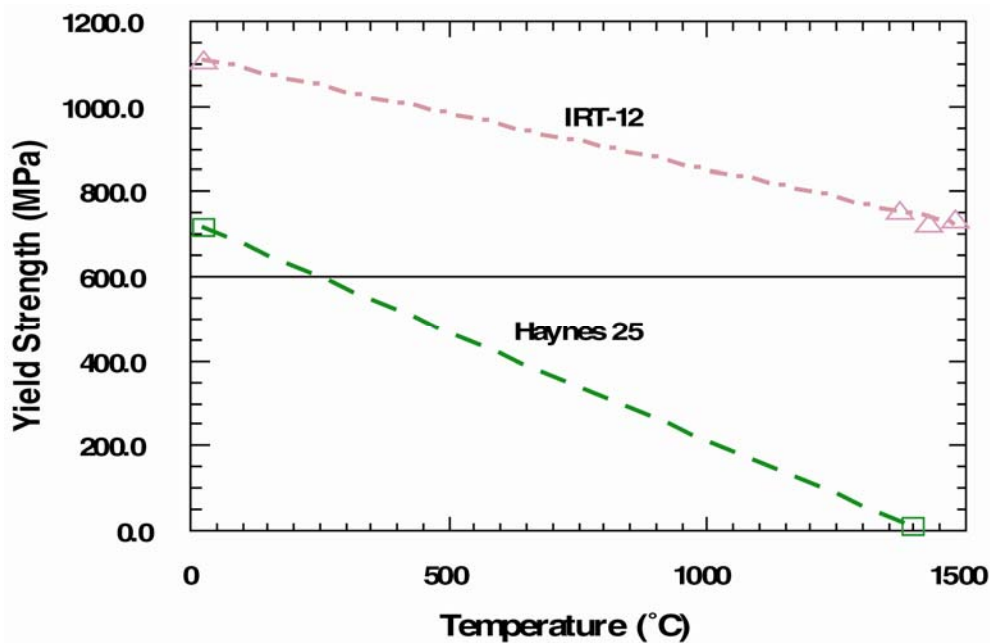


Figure 13. Comparison of ITR-12 and Haynes-25 Alloys

#### 4.1.2 Oxidation Resistance

The Iridium alloy was tested for oxidation resistance by exposing it to air at 1700 K for 10 min at 1 atm. Weight changes for several candidate alloys are given in Table 1. A corrosion-resistant “superalloy,” Haynes 25, is shown as a reference. “Pre” and “post” photographs are shown in Fig. 14. For Haynes 25, thick oxide layers were formed, which cracked and spalled during cooling from 1427°C. The net weight change of the Haynes 25 specimen was the result of a balance between the weight gain from oxide scale formation and the severe spalling of the oxide layer. A severe distortion of the Haynes 25 surfaces is observed, whereas a very thin layer of oxides is observed on the IRT-12 sample. The Haynes 25 shows serious degradation with deep pockmarks, and it experiences a mass loss of 12.45 mg/cm<sup>2</sup>. The Iridium alloy shows a very thin film with a mass loss of 0.42 mg/cm<sup>2</sup>.

**Table 1. Weight Changes for Candidate Alloys**

<b>Alloy Number</b>	<b>Weigh Changes for Candidate Alloys (mg/cm<sup>2</sup>)</b>
<b>IRT-1</b>	<b>-0.27</b>
<b>IRT-2</b>	<b>+0.12</b>
<b>IRT-3</b>	<b>-0.04</b>
<b>IRT-8 (5% Zr)</b>	<b>-1.12</b>
<b>IRT-10 (5% Hf)</b>	<b>-0.42</b>
<b>IRT-11 (4% Zr)</b>	<b>-0.25</b>
<b>IRT-12 (4.5% Zr)</b>	<b>-0.42</b>
<b>Haynes 25</b>	<b>-12.45</b>

### Haynes 25

### Ir alloy: IRT-8



- **Comparison of Unoxidized and Oxidized Specimens (Exposed at 1427°C for 10 min)**

**Figure 14. Results of Oxidation Test of Iridium Alloy**

The superiority of the Iridium alloy to Haynes 25 is evident from both appearance and weight change. A second test method was utilized in which a burner was used to subject the specimen to a flowing gas. However, the only practical way to do an oxidation test at 600 MPa is to test a nozzle in the A2Lite (described in a subsequent section). This is also true for erosion testing.

#### **4.1.3 Thermal Shock Resistance**

The thermal shock resistance of Ir-Zr alloys was characterized using a cylindrical specimen having a small diameter of 0.24 mm. The specimen was first held at 1427°C for 10 min and then quenched immediately in stirred water. Optical examination showed no indication of oxide coatings or microcracks on specimen surfaces, indicating resistance to thermal shock. The mechanical properties of this oxidized and quenched specimen were evaluated by compression testing at 1427°C. The alloy specimen exhibited a yield strength of 720 MPa and an ultimate strength of >1110 MPa at 1427°C, the values of which are comparable to those unquenched specimens. It is thus concluded that the

1427°C pre-oxidation and thermal shock treatment have no adverse effects on the mechanical properties of the alloy.

Thermal stresses are expected to increase with specimen size. To further characterize the thermal shock resistance, a 0.05-in.-diam by 1.6-in.-long alloy ingot was first air oxidized for 10 min at 1427°C and then quenched immediately in water. Optical examination reveals no apparent oxide scales or microcracks formed on the ingot surface. On the basis of all these results, it is concluded that the thermal shock resistance of the Ir-Zr alloy is very good and should be of no concern for structural use at high temperatures.

#### 4.1.4 Thermal Properties

Thermal properties were determined over the temperature range from 20 to 1427°C. The thermal diffusivity increases with temperature up to 500°C and then remains constant. Specific heat increases relatively linearly with temperature. Properties at the end points of the range are shown in Table 2.

**Table 2. Thermal Properties**

<b>Thermal Properties at:</b>	<b>20°C</b>	<b>1427°C</b>
Density *	22.12 gm/cm <sup>3</sup>	22.12
Thermal Diffusivity	0.145 cm <sup>2</sup> /s	0.195
Specific heat	0.136 J/gm/K	0.172
Thermal Conductivity [computed from $\kappa = \alpha \rho C_p$ ]	43.6 W/m/K	74.2

\* 10 measurements, uncertainty 0.1 percent (thermal expansion nonsignificant)

#### 4.1.5 Thermal/Stress Modeling

##### Introduction

This section summarizes the results of an analytical study of the proposed nozzle material (Iridium alloy) for the high-temperature-and-pressure environment of 2880 R (1600 K) and 300,000 psi (2068 MPa). The nozzle material is made of a special Iridium alloy and is being manufactured by ORNL. The nozzle inside contour and the heat and structural loads were obtained from the A2Lite/RDHWT Project.

The nozzle was analyzed for a dynamic thermal load and a static pressure load. ORNL determined the thermal properties of the new material, and they are as reported in the thermal model section. The nozzle sketch and its housing are shown in Fig. 15. This assembly slides into another cylindrical housing and is shown modeled in Fig. 16. Since



the outer two shells are the same material, a uniform cylindrical boundary was easier to model.

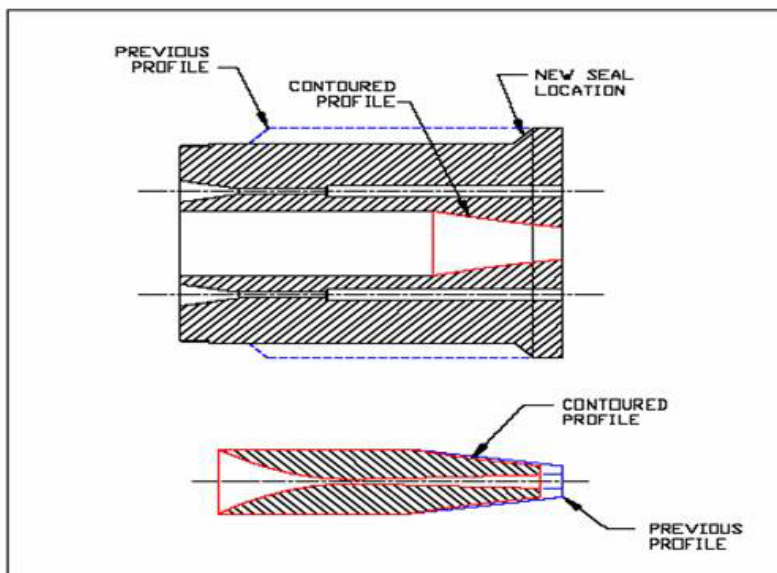


Figure 15. Sketch of Nozzle

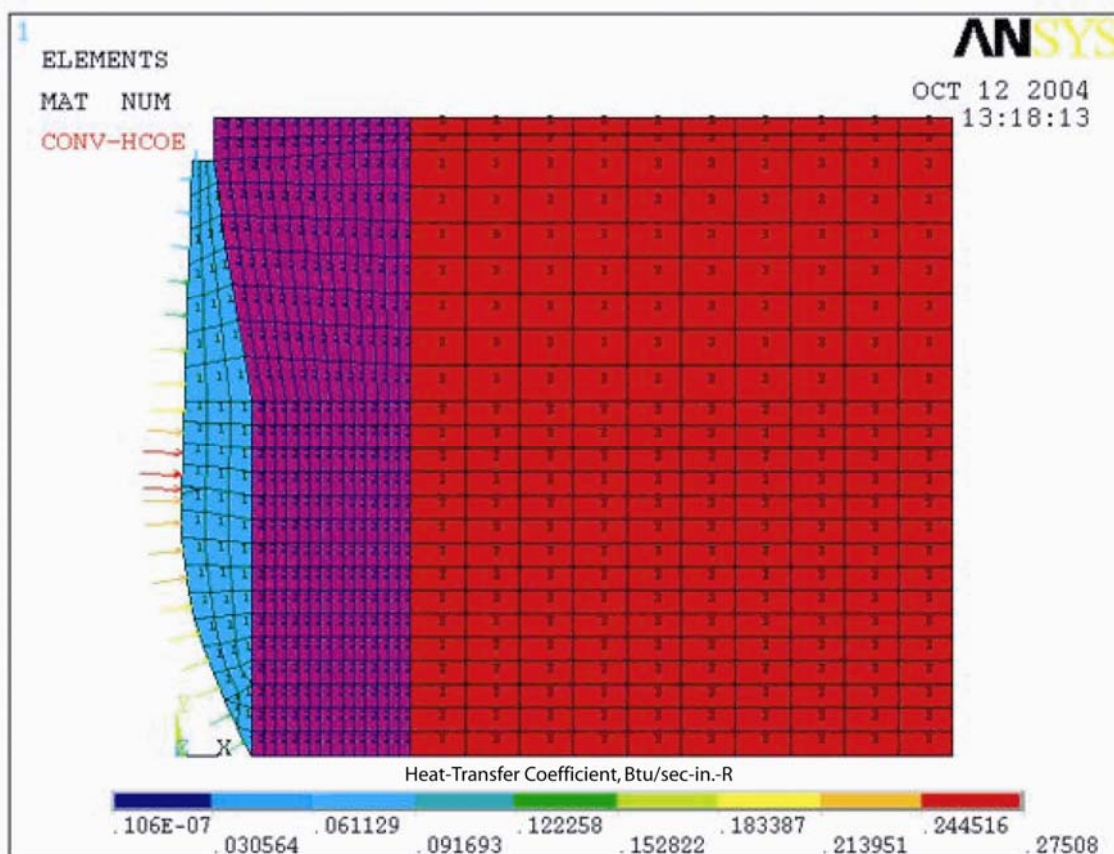


Figure 16. FEA Thermal Model

### Method of Analysis

The conventional method of analyzing this type of high-temperature nozzle assembly is to model the stress/strain curve of the various materials and perform an elastic/plastic finite element analysis (FEA) structural analysis per the methods in the ANSYS program. Since the nozzle material is under development and the stress/strain curve at temperature is not available, another method of analysis has been used. The life of the nozzle was approximated by the strain-life method as proposed in a paper in the December 1962 issue of Journal of Basic Engineering by Tavernelli and Coffin and adopted by the ASME for use in Boiler and Pressure Vessel design work.

### Thermal Model

An FEA thermal model of the nozzle section was created using ANSYS plane55 thermal elements in an axisymmetric configuration as shown in Fig. 16. The x-axis is radial, and the y-axis is axial. The three-layered vessel consists of an inside layer of Iridium alloy, with the second and third layer made of Am-350 steel. No special fits were applied to the various layers.

The Iridium alloy material properties used at temperature were reported by ORNL in their November 03 monthly report and are listed in Table 3, below (with conversions to the English system by the author). The steel thermal properties were taken from Mil HDBK-5H and also are listed in Table 3. It was assumed that Poisson's ratio would remain constant with temperature for both materials and was approximately 0.3.

**Table 3. Material Properties Used in FEA Thermal Model Analysis**

Material	Temp. (°R)	Specific Heat (btu/lbm-°F)	Conductivity (btu/sec-in-°F)	Density (lbm/in.3)	Ultimate Strength (ksi)	Yield Strength (ksi)	Modulus of Elasticity (ksi)	Coefficient of Expansion (in./in.-°R)
Iridium (IR12)	500	0.0325	5.84e-4	0.799	415	139	76000	6.4e-6
	3000	0.0411	9.9e-4	0.799	136	83	55000	6.4e-6
Am-350 steel	500	0.12	2.1e-4	0.282	360	350	27000	6.2e-6
	3000	0.12	2.8e-4	0.282	~55	~50	10000	6e-6

The ends and the outside diameter were all considered insulated so that no heat was transferred through these surfaces. The conditions given below are somewhat conservative, but they will provide an upper limit.

The following transient heat load was applied to the nozzle:

The model was preheated to 1350°R (750 K). The heat load was applied as a step function for 1 s and adiabatic for 4 s, establishing maximum thermal loads. A recovery temperature of 2880°R with throat heat-transfer coefficient of 0.275-btu/in.<sup>2</sup>-R-s was used at the throat. The equation used for determining the throat heat-transfer correlation is taken from Ref. 4:

$$h(\text{btu/ft}^2/\text{s/k}) = 0.0043 * (P_o^{0.74}) * (T_o^{0.31}) \quad \text{where } P_o \text{ is in atm and } T_o \text{ is in K.}$$

One-half the throat value of the heat-transfer coefficient was used at the entrance of the nozzle for the subsonic side. The supersonic side was estimated on the basis of area ratio, and the heat-transfer value used was assumed to be linear from the throat to the exit, where a value of  $0.2\text{-Btu to in.}^2\text{-}^\circ\text{R-s}$  was used. The total duration of the test was 5 s. Figure 16 shows the heat-transfer coefficient distribution and the size and shape of the FEA model.

### Thermal Results

The analysis shows in Figs. 17 and 19 that the maximum temperature of the iridium alloy on the gas side occurs at 1 s and is  $2864^\circ\text{R}$ . A maximum thermal gradient (denoted by “del” on the plot) through the thickness of the iridium was determined to occur at less than 0.1 s and was  $1487^\circ\text{R}$ . Figure 17 shows these values plotted as a function of time. Figure 17 also shows the lag in temperature vs. time for the outer steel layer and shows that it experiences very little temperature increase in 5 s. At the steel interface the temperature rise in 5 s is only  $1^\circ\text{R}$ , showing that location is not affected thermally by the heat transfer. (It is not seen on the plot because the blue color hides it.)

The temperatures for the various times listed previously are shown on the FEA model in Figs. 18 through 20 for reference. The maximum gradient through the nozzle historically occurs at or near the throat, as substantiated by Fig. 19.

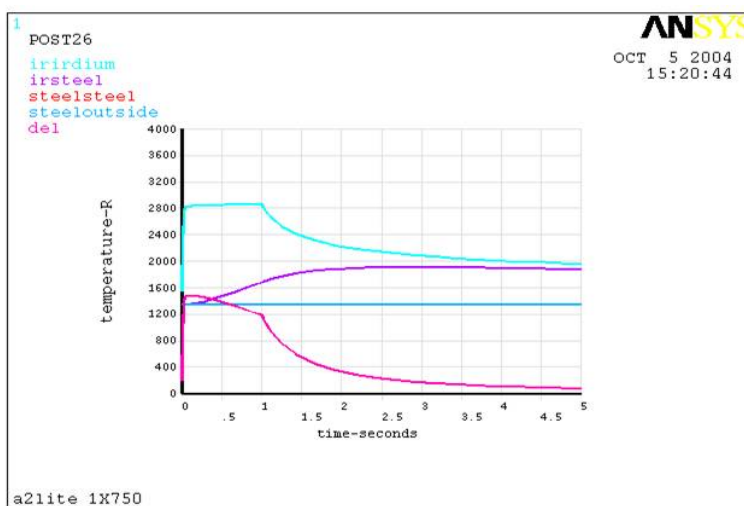


**Figure 17. Plot of Temperature vs. Time at the Throat Axial Location**

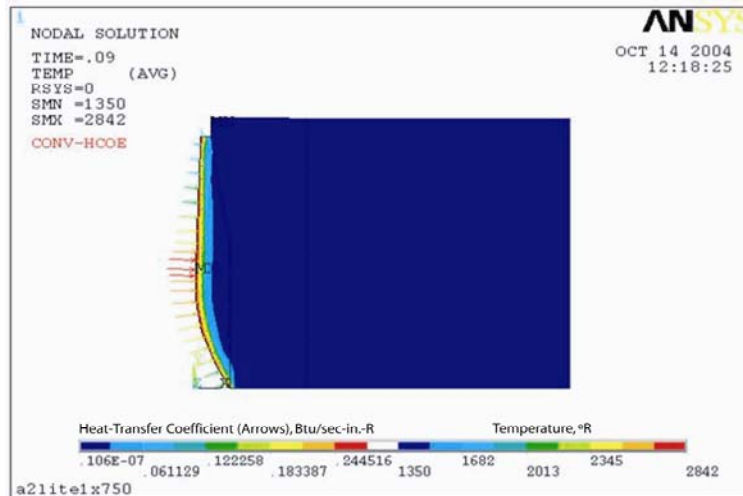


Figure 18. Assembly Temperature Distribution at 0.09 s

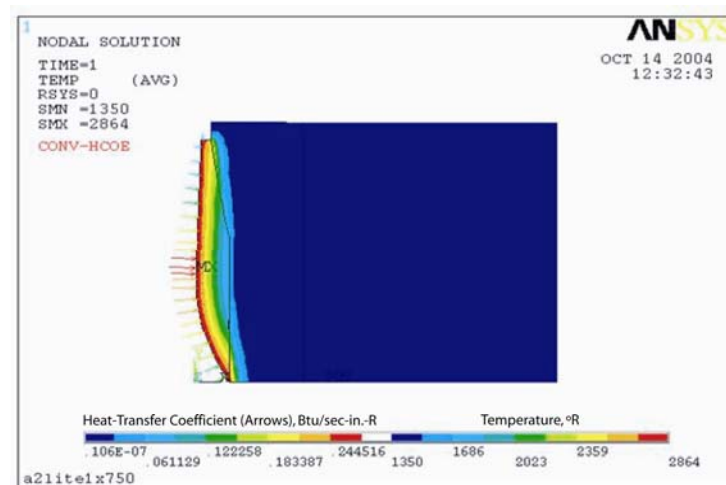


Figure 19. Assembly Temperature Distribution at 1 s

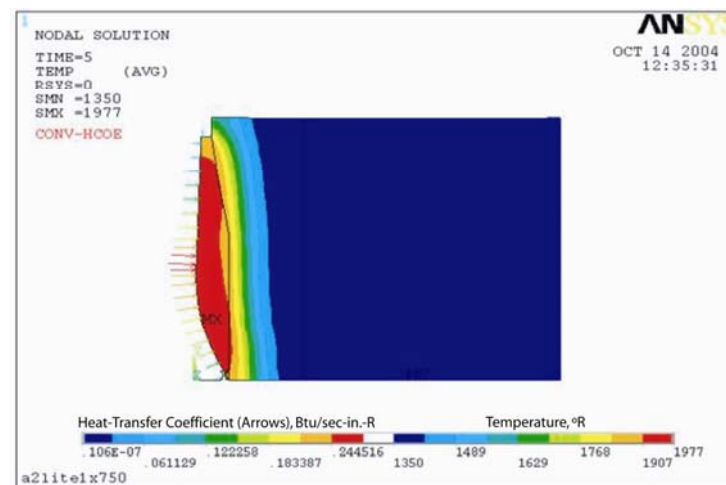


Figure 20. Assembly Temperature Distribution at 5 s

## Structural Model

Figures 21 and 22 show the structural model with pressure load distribution and confirmed temperature distribution for the assembly. The operating pressure was 300,000 psi. It is assumed that the flow is sonic at the throat and that the pressure is approximately only one-half the inlet value at the throat and downstream. Figure 21 confirms that the correct temperature distribution was analyzed, as was the thermal solution in Fig. 18.

The FEA structural analysis consisted of using the FEA thermal model and changing the elements to type plane42 structural and adding contac12 elements (shown in Fig. 21) to solve the mechanical/thermal stress analysis. One end of the assembly was restrained in the axial direction, and axisymmetry was used.

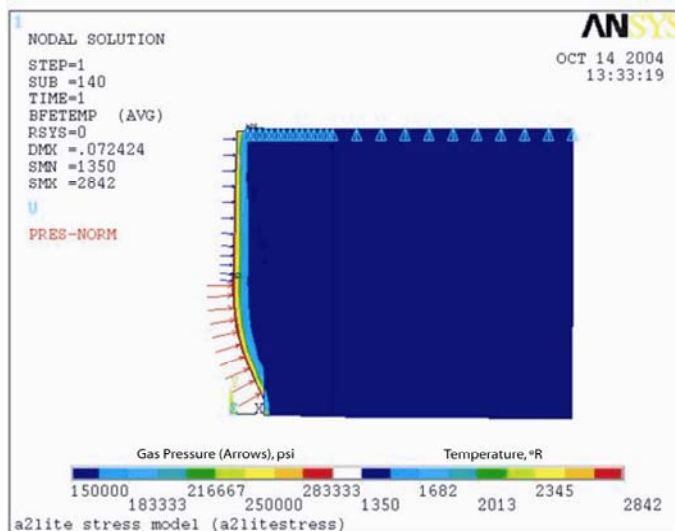


Figure 21. Confirmed Thermal Distribution at 0.09 s

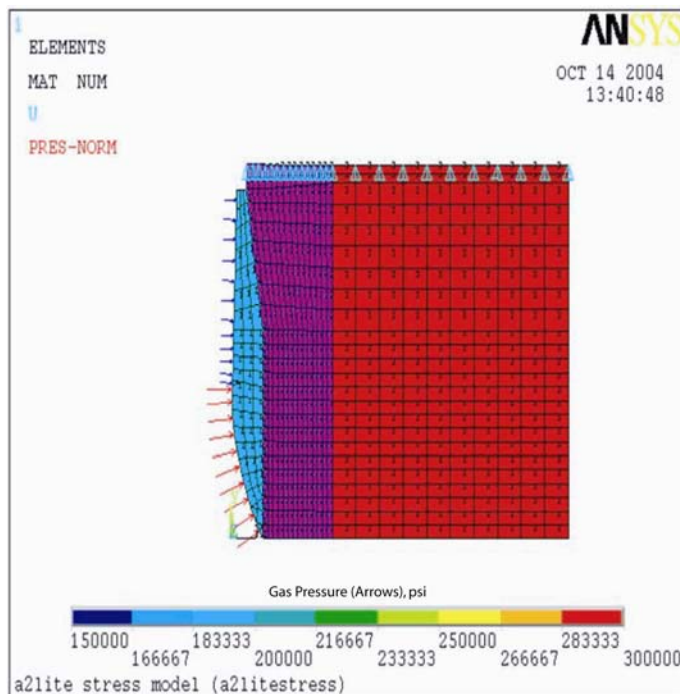


Figure 22. Pressure-Loaded Stress Model

## Structural Results

The FEA in Figs. 23 and 24 shows that the stress levels are well over the yield strength (Table 1) at temperature and that a plastic analysis needs to be made for the design. However, mechanical properties do not yet exist for the iridium at temperature. Therefore, the strain-life method is used to make an estimate of the life of the nozzle. This method uses the fictitious stress as calculated by an elastic analysis to predict the life of the component. The task of this project was to determine the number of cycles before failure.

To use the approximation of the strain-life method, the principle stresses have to be determined. Then the largest principle stress is used for the approximation. With the components assembled, it is difficult to tell which material the stress belongs to. Therefore, just the Iridium material results were also plotted to give a more accurate prediction.

Figures 25, 26, and 27 show the three principle stresses for the assembly. The object is to find the largest principle stress at the throat. Figure 27 shows that the largest is near -1,880 ksi. The yield strength of the material at temperature is subtracted from this fictitious stress.

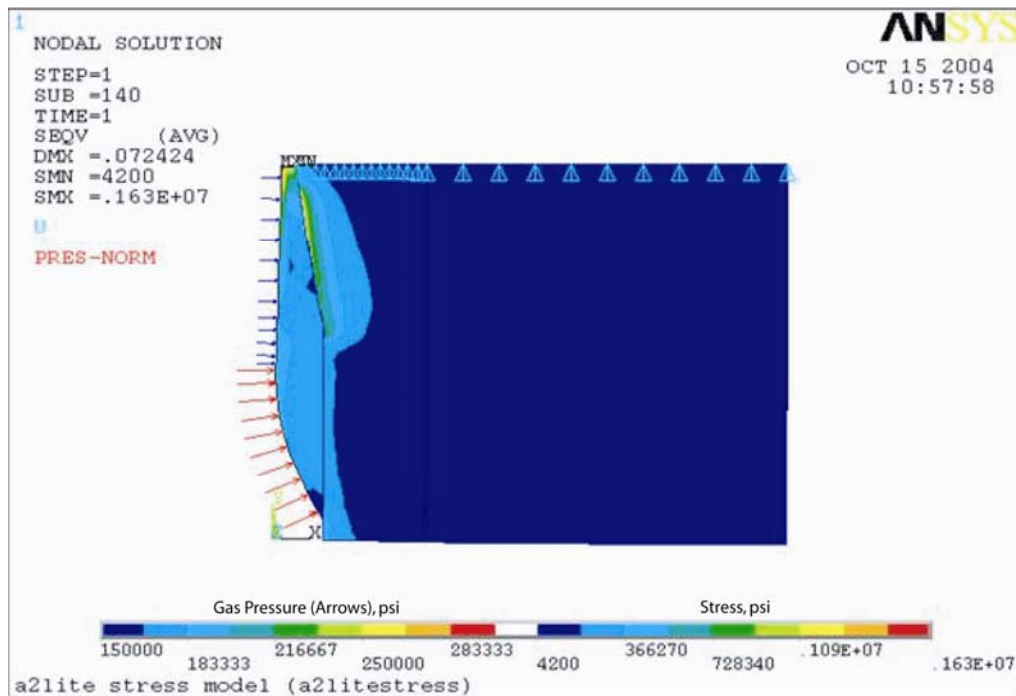
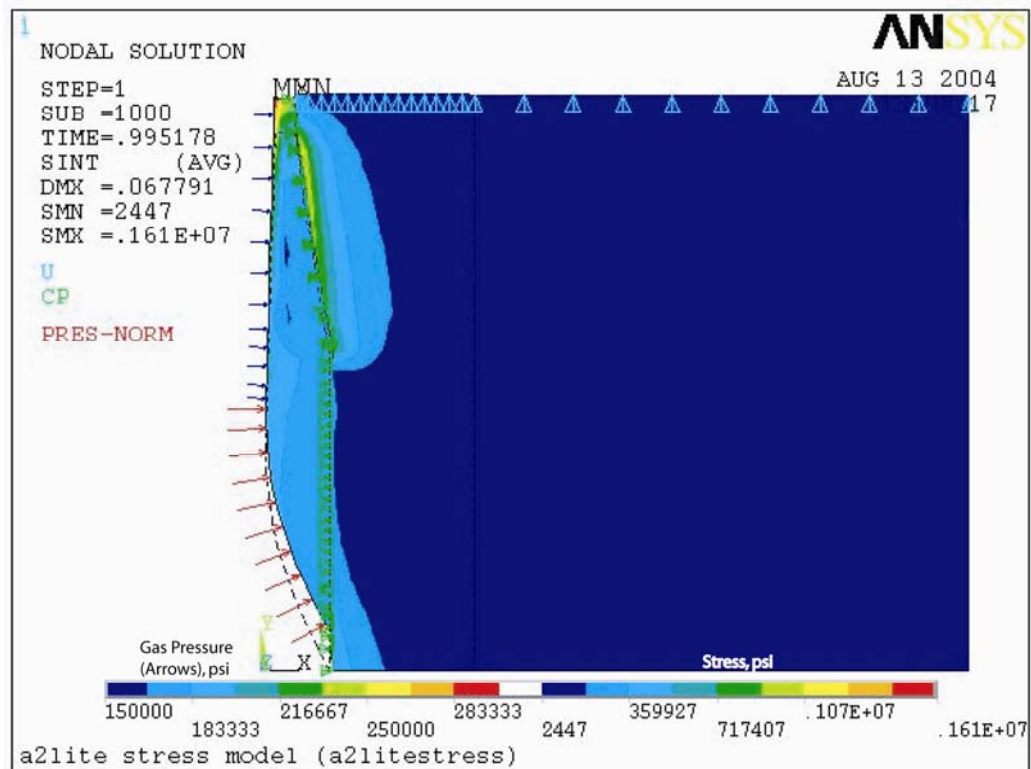
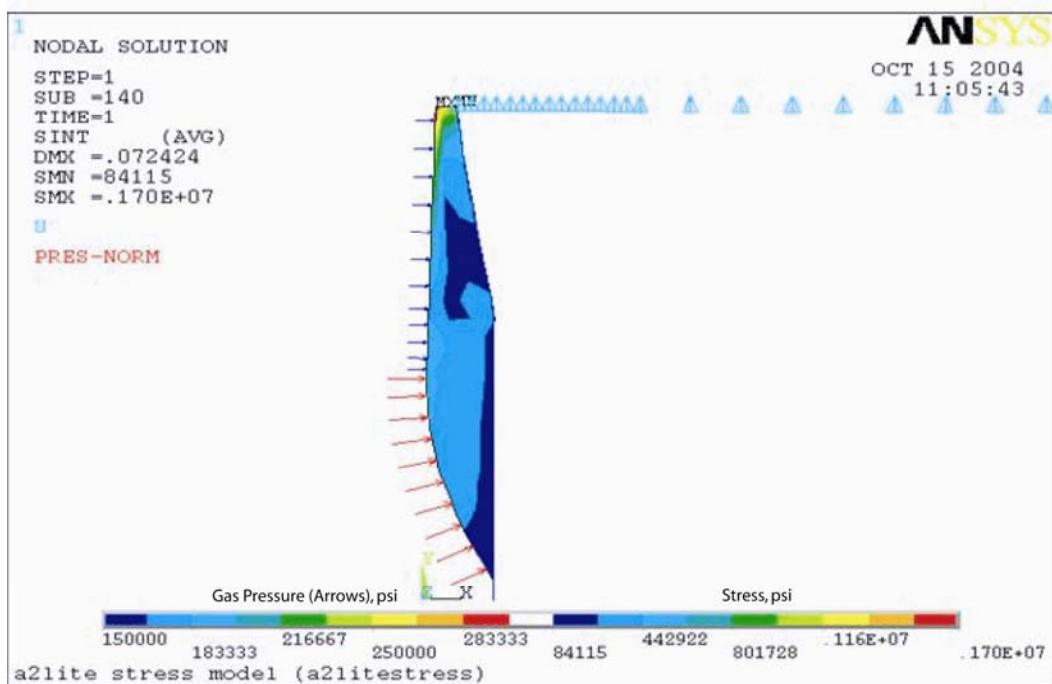


**Figure 23. Equivalent Stress Compared to Yield Strength**



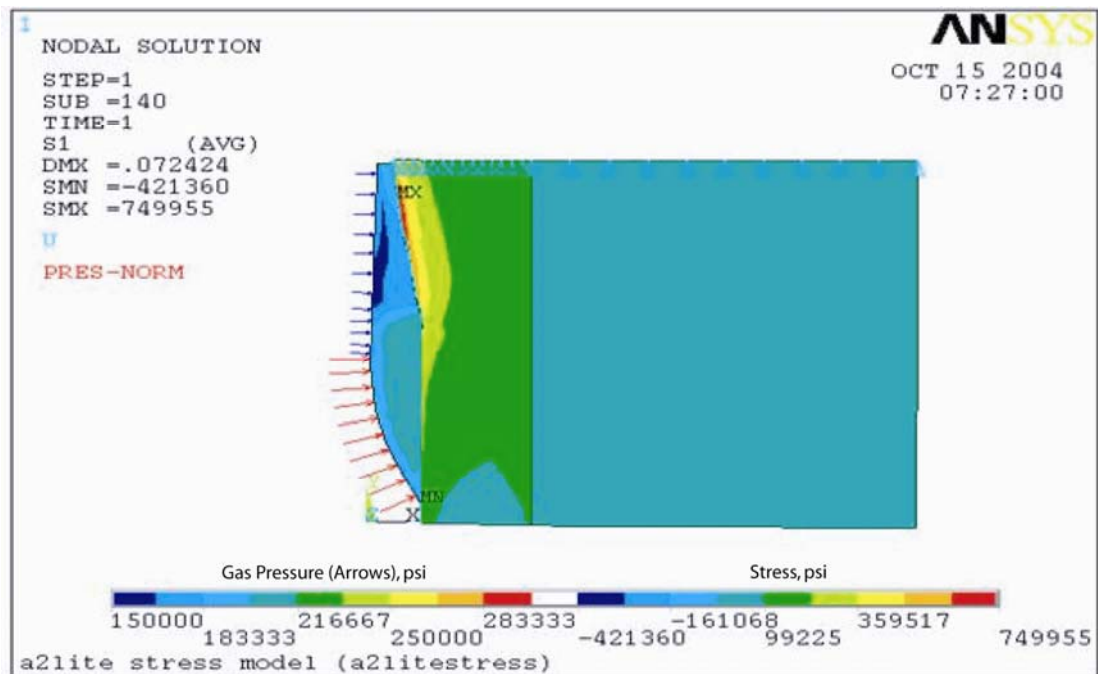


a. Entire nozzle structure

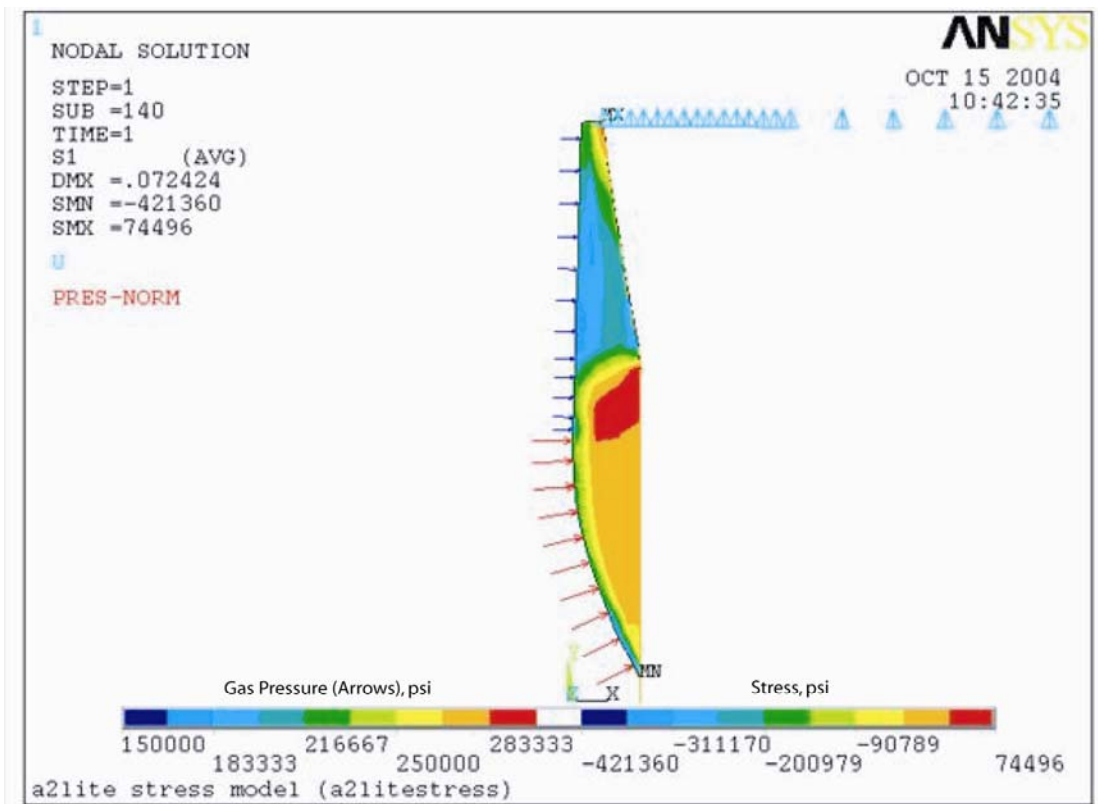


b. Nozzle liner only

Figure 24. Stress Intensity



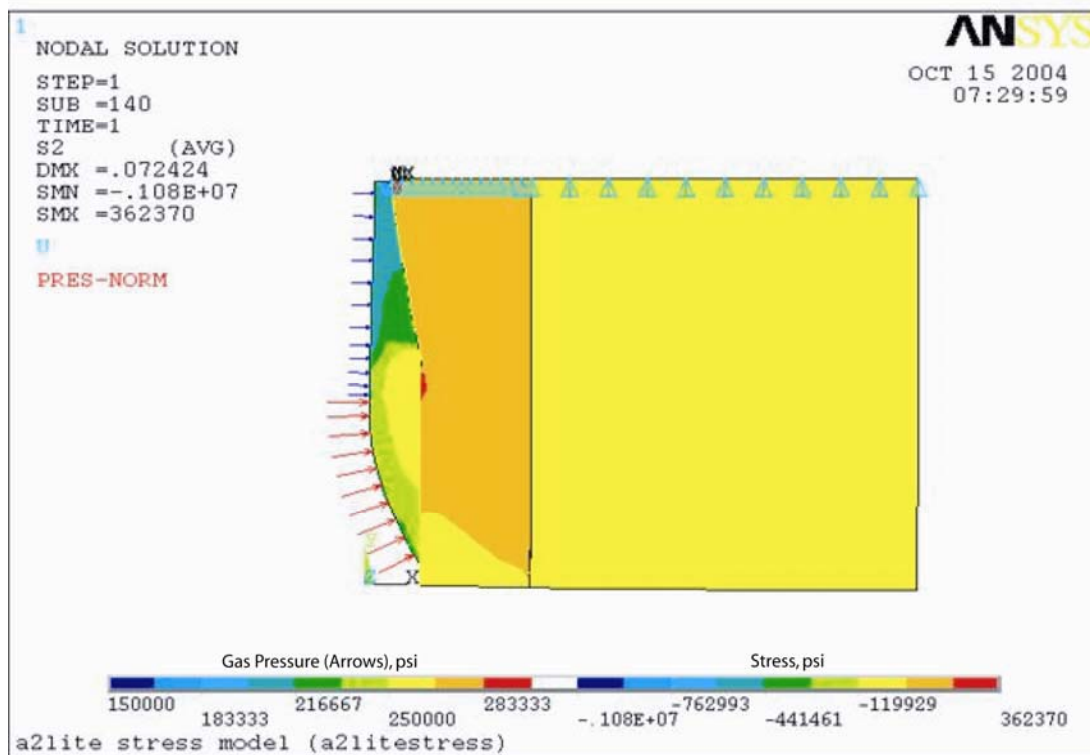
a. Entire nozzle structure



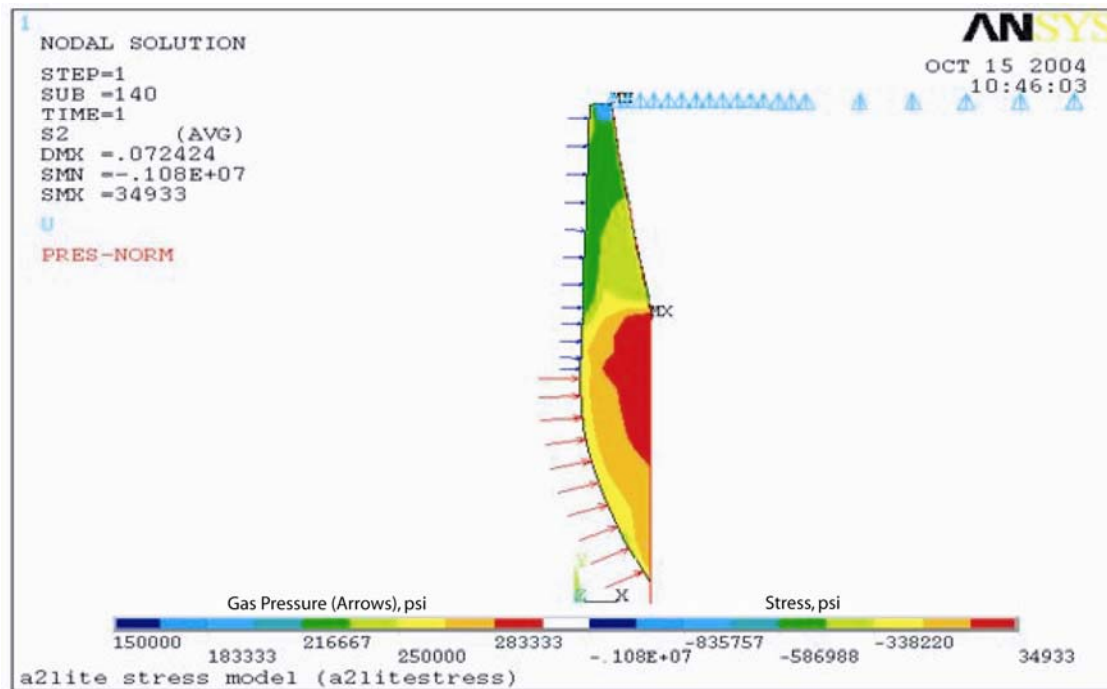
b. Nozzle liner only

Figure 25. Principal Stress Distribution for Direction 1



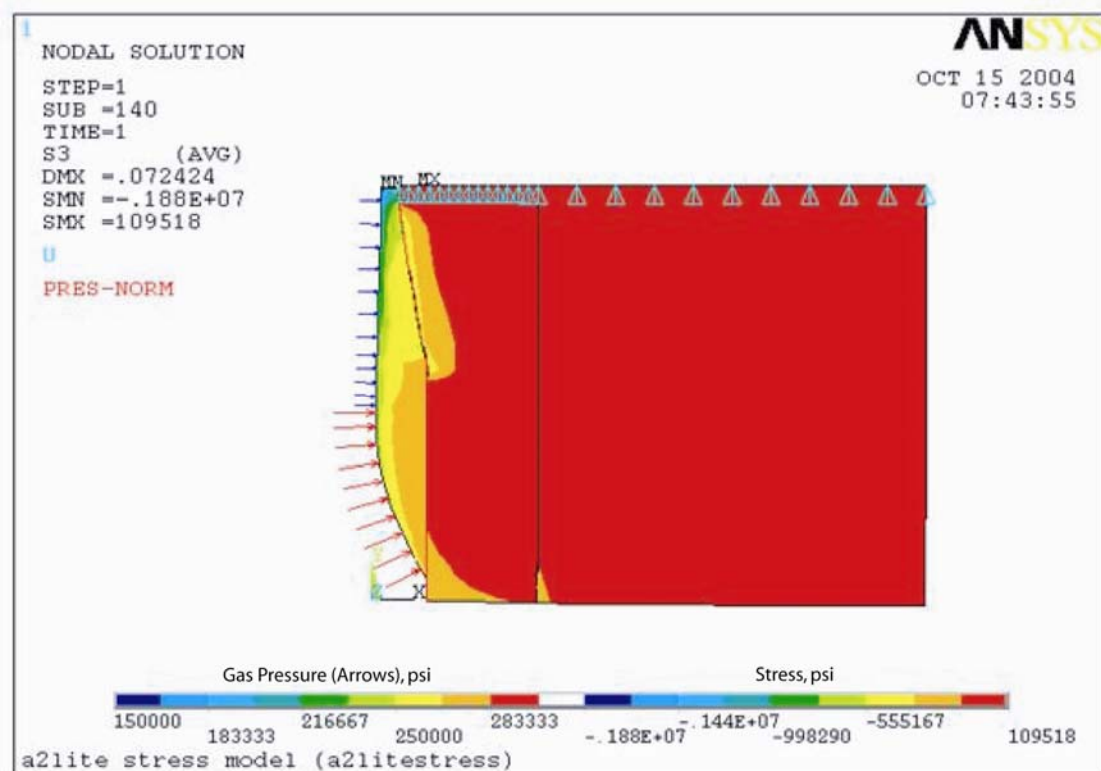


a. Entire nozzle structure

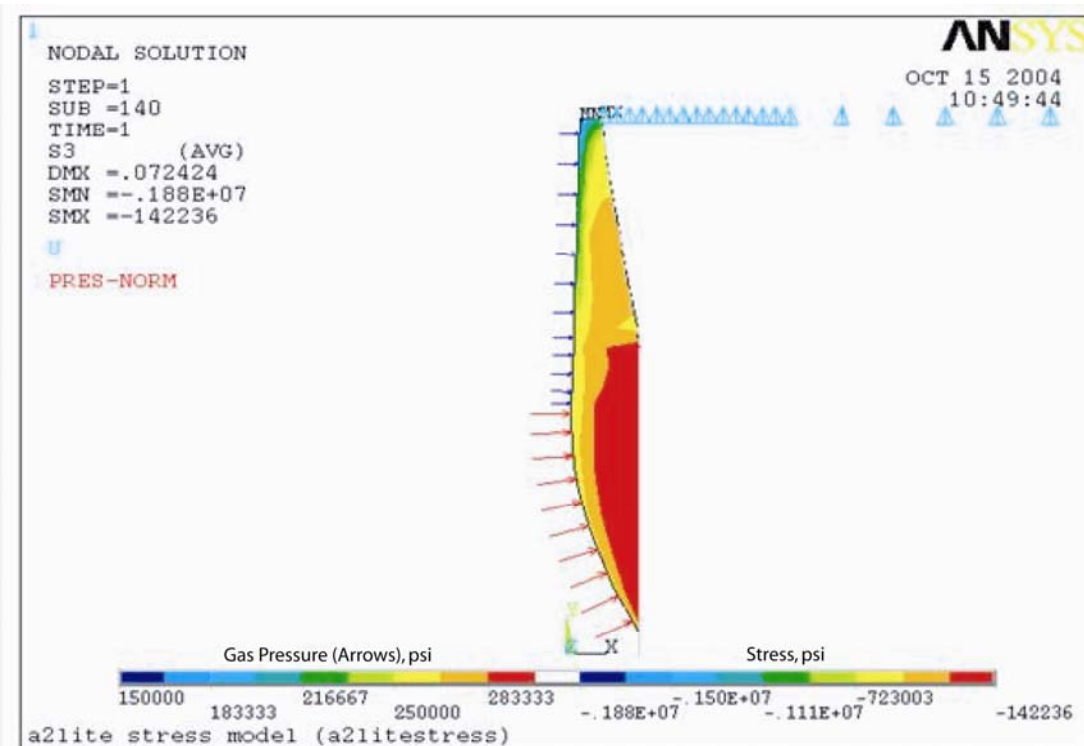


b. Nozzle liner only

Figure 26. Principal Stress Distribution for Direction 2



a. Entire nozzle structure



b. Nozzle liner only

Figure 27. Principal Stress Distribution for Direction 3

Then the remainder is divided by the modulus of elasticity at temperature, with the result being the fictitious plastic strain. Then, using the strain-life relation:

$$N = (0.36 / \text{fictitious plastic strain})^2$$

gives the predicted life (in cycles) of the material. For this case the predicted life of the Iridium liner per this method is estimated to be six cycles.

The previous analysis gives the life based on a stress/strain relationship. The thermal shock should also be considered to check for surface damage at each particular run. The conventional thermal shock equation is:

$$\Delta T = \frac{\text{ultimate strength} \cdot (1 - \text{poissons ratio})}{(\text{expansion coefficient} \cdot \text{modulus of elasticity})}$$

all at temperature conditions (average).

For this material the allowable gradient was determined to be 270°F. Figure 17 shows a temperature gradient at the throat of about 1000°F (1487°R). Thus, there should be some thermal cracking showing up right away, but failure should not occur until six cycles have been reached.

In summary:

1. The Iridium material should last approximately six cycles for an environment of 2880°R (1600 K) and 300,000 psi (2068 MPa) applied for one second.
2. There should be surface damage after every shot.

#### **4.1.6 Nozzle Insert Fabrication**

Ingot fabrication by arc melting and drop casting was found to be a convenient way to produce small ingots of the alloy for characterization tests. However, it was known that the size of ingot that could be produced by this method was limited. An A2Lite nozzle insert requires an ingot 0.8 in. in diameter by 3.0 in. long. The arc-melt/drop-cast hardware had to be somewhat redesigned to cast an ingot this large. It was subsequently determined that a nozzle could be machined by EDM. However, unacceptable porosity was discovered during the machining process. Therefore, an alternate casting method was sought that would allow large ingots to be cast.

Drip casting was selected as an alternate candidate method for larger ingot preparation. This procedure was carried out at ALD Vacuum Technologies, in Germany. This method employs local melting and solidification as shown in Fig. 28. An imperfectly shaped alloy electrode is prepared as a material source. The electrode is melted and drips into a water-cooled mold with a receding bottom. One electron beam was used to melt the electrode while a second electron beam was used to control the rate of solidification in the mold. Gas bubbles tend to come to the top of the ingot given sufficient time before solidification, thus tending to minimize porosity. It appears that the second electron beam did not supply sufficient energy and thus allowed the melt to

solidify quickly, consequently trapping porosity. Considerable effort was expended, including an HIP process, to salvage the ingot. However, the first attempt was ultimately unsuccessful because of porosity.

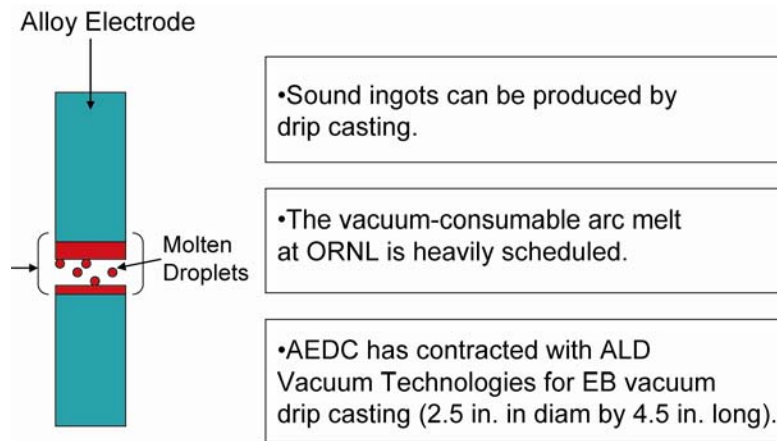


**Figure 28. Schematic of Drip-Casting Technique**

A second attempt was made using a vacuum arc remelting technique at ORNL. The procedure is similar to that shown schematically in Fig. 28 except that an electric arc, rather than an electron beam, is used to melt the electrode. An ingot 1-7/8 in. in diameter and 4 in. long was successfully produced (see Fig. 29). Three A2Lite nozzles can be machined from this size ingot. A nozzle has been machined with an EDM technique (see Fig. 30).

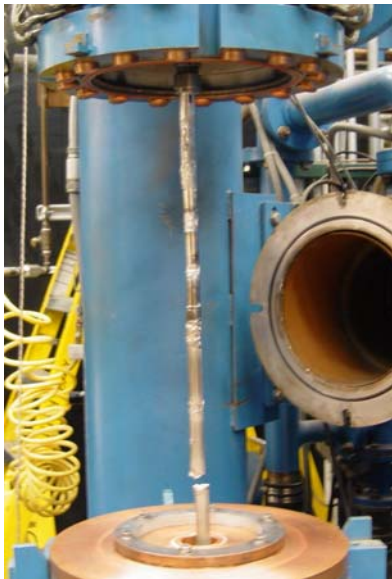


**Figure 29. Vacuum Arc Remelting Process Used to Produce Alloy Ingot**

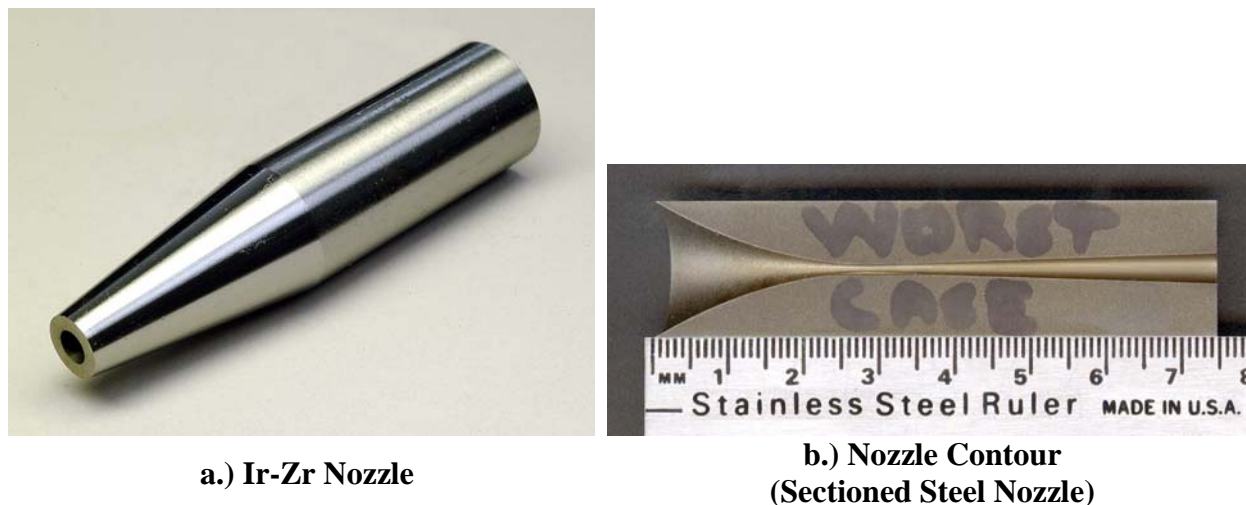


**Figure 30. Iridium Alloy Nozzle for Testing in the A2-Lite**

#### 4.1.7 Future Nozzle Testing

The A2Lite<sup>2</sup> (shown in Fig. 31) is a pilot ultra-high-pressure air source developed under the RDHWT program and is located at MSE-TA in Butte, Montana. The pressure vessel is a three-layer compound cylinder designed to operate at 750 K at pressures up to 2300 MPa. Pressurization is accomplished by means of a differential piston (100:1 area ratio, as shown in Fig. 31). A nozzle can be mounted at the opposite end of the pressure vessel. (In Fig. 31 the piston is located at the right-hand end of the pressure vessel, the nozzle at the left end.) This device was built with two objectives in mind: a) to demonstrate that such a device could be built and operated at this pressure and scale, and b) to serve as a test bed for nozzle survivability experiments for the RDHWT nozzles.

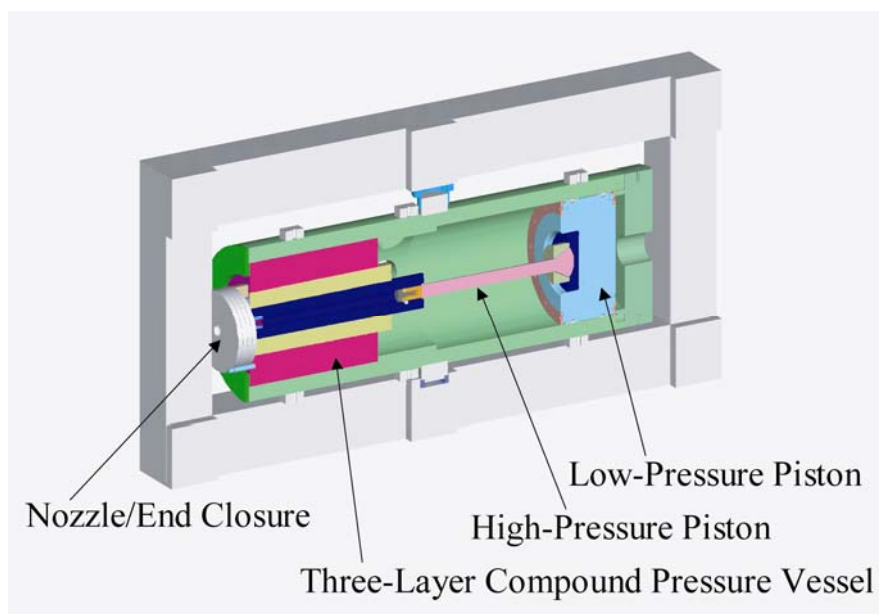


**Figure 31. Schematic of A2Lite**

A nozzle throat insert compatible with the A2Lite has been fabricated from the Ir-Zr alloy described here. Original plans were to test this nozzle at pressures up to 2300 MPa in the A2Lite following the initial planned tests with a maraging steel nozzle. It now appears that the A2Lite will not be available for the Ir-Zr nozzle tests in the foreseeable future. As an alternative, a test in the AEDC H1 arc heater is being planned. With proper mixing air, the correct recovery temperature can be achieved, but the pressure level will fall short of the RDHWT requirement.

## 4.2 Mo-Si-B ALLOY DEVELOPMENT

Development of a second candidate material was deemed important a) as a backup for the RDHWT application and b) as a potential candidate material for a Tunnel 9 nozzle insert. Mo-Si-B exhibited excellent potential for strength at temperature, but it lagged Iridium with respect to oxidation resistance.

### 4.2.1 Composition, Strength, and Fracture Toughness

Mo-Si-B alloys have been shown to exhibit high strengths at elevated temperatures (Refs. 6, 9, and 10). Figure 32 shows a section of the ternary Mo-Si-B phase diagram indicating one alloy composition of interest, namely Mo-10Si-14B (numbers refer to atomic percent). This composition consists primarily of a mixture of a Mo solid solution phase and the ternary  $\text{Mo}_5\text{SiB}_2$  (T2) phase. In this work, compositions in the Mo-Mo<sub>3</sub>Si-Mo<sub>5</sub>SiB<sub>2</sub> region are considered. If the composition is moved towards the Mo phase, the Mo volume fraction increases. If the composition is moved downwards, the Mo<sub>3</sub>Si phase is formed at the expense of the T2 phase. The intermetallic phases Mo<sub>3</sub>Si and Mo<sub>5</sub>SiB<sub>2</sub> are much stronger than the Mo phase, but they are brittle. Consequently, there is a trade-off between strength and fracture toughness. If the volume fraction of the Mo phase is reduced, the strength increases, whereas the fracture toughness decreases.

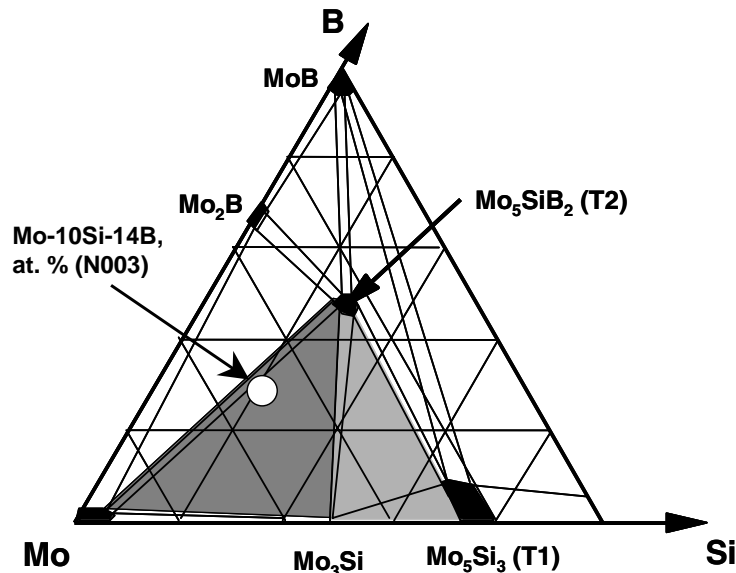
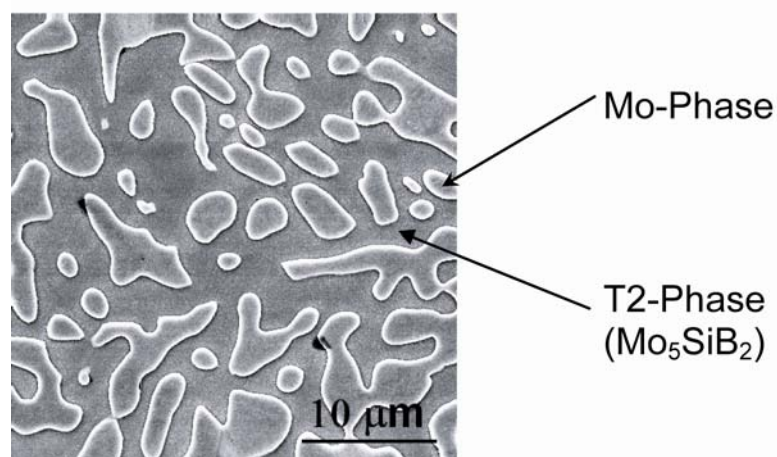


Figure 32. Schematic Section of the Mo-Si-B Phase Diagram at 1600°C



#### 4.2.2 Processing by Melting and Casting

An alloy with the composition Mo-10Si-14B (at. %) was prepared by arc-casting on a water-cooled copper hearth in argon, followed by drop-casting into a water-cooled cylindrical copper mold with a diameter of 12.5 mm. Figure 33 is a scanning electron micrograph of this alloy showing the T2 phase  $\text{Mo}_5\text{SiB}_2$  (dark) and the Mo solid solution phase (bright).



**Figure 33. Scanning Electron Micrograph of the Microstructure of a Mo-10Si-14B at. % Specimen after Casting and Annealing (1 Day/1600°C/Vacuum)**

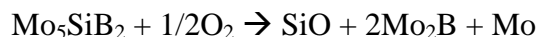
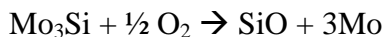
If processing is carried out by melting and casting, the Mo solid solution phase with its high melting point nucleates first. The brittle T2 phase ( $\text{Mo}_5\text{SiB}_2$ ) forms once the Mo solid solution phase has nucleated, and the T2 phase tends to be continuous. The brittle T2 matrix implies a low fracture toughness and essentially no room-temperature ductility. Mo-10Si-14B alloys prepared by melting and casting are extremely strong in compression. In compression at room temperature, they fail at 2790 MPa. However, failure occurs without plastic deformation; the specimens shatter. When tested in flowing argon at 1700 K in compression, these alloys deform plastically with a 0.2-percent yield stress of 1000 MPa.

Nozzle inserts for the A2-Lite wind tunnel (where initial nozzle survivability tests might be conducted) require blanks with a diameter of  $\approx 19$  mm and a length of  $\approx 80$  mm. Experiments were carried out to determine whether blanks of this size can be fabricated by arc-melting and drop-casting. A sufficiently large ingot of Mo-10Si-14B (at.%) could be produced. However, it was judged too brittle for the nozzle application. A composition with significantly reduced Si and B concentrations, Mo-7Si-7B (at.%), i.e., a much larger Mo solid solution volume fraction, was selected in order to increase the fracture toughness. However, it could not be dropped into a copper mold since the liquid was too viscous (because of the high Mo concentration). Attempts were then made to cast an alloy with the composition Mo-8Si-11.2B, at.%. After five attempts, an ingot over 80 mm long with a diameter of 19 mm was obtained. In order to obtain this ingot, excess material had to be used. A total of 750 g of material had to be used to fabricate the cylindrical

ingot, which weighed approximately 300 g. If smaller amounts were used, the cylindrical copper mold would not fill properly. The head of the ingot did not show a central depression or pipe. This indicates that there was no material flow to accommodate shrinkage during solidification. In an attempt to reduce porosity, the ingot was isostatically hot-pressed in argon at a temperature of 1700°C and a pressure of 207 MPa for four hours. As expected, the microstructure consisted of large primary molybdenum dendrites with typical widths of 10  $\mu\text{m}$  and a fine-scale Mo-Mo<sub>5</sub>SiB<sub>2</sub> eutectic. However, the casting porosity was not removed. Examination showed that the porosity in the center of the ingot varied widely along its length. In some locations there was hardly any porosity, whereas in other locations the porous zone in the axis of the ingot had a diameter of approximately 3 mm. Also, there was evidence of longitudinal macrocracks. Based on these results, it is concluded that casting of 19-mm (0.75-in.)-diam cylinders of Mo-Si-B alloys is not feasible even though smaller ingots can be successfully cast.

### 4.2.3 Processing by Powder Metallurgy

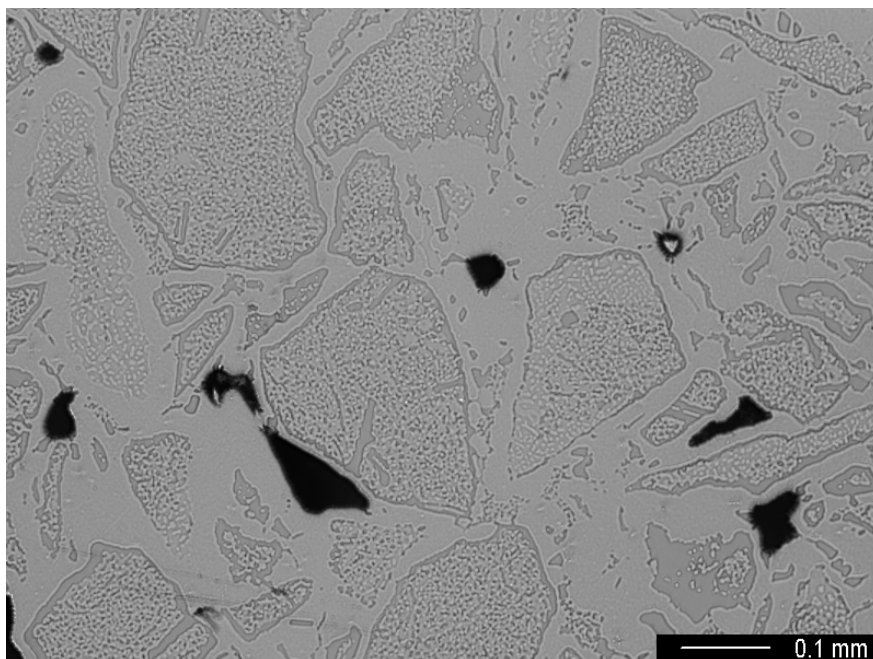
Whereas melting and casting tends to result in microstructures consisting of particles of Mo solid solution in an intermetallic matrix (see Fig. 32), powder metallurgical processing offers the possibility of creating microstructures consisting of intermetallic particles such as Mo<sub>5</sub>SiB<sub>2</sub> and Mo<sub>3</sub>Si in a matrix of Mo solid solution. One way to do this is to pulverize cast ingots, coat the powder particles with Mo, and follow with consolidation. The Mo-Si-B particles can be “coated” by removing Si from their surfaces by annealing in vacuum (Ref. 11). This process leaves behind Mo, which forms an Mo solid solution coating on the particles. The Si is either removed as elemental Si, or it reacts with residual oxygen in the vacuum system to be removed as volatile SiO according to:



Silicide powder with the composition Mo-20Si-10B, at. % (i.e., a mixture of the phases Mo<sub>3</sub>Si and Mo<sub>5</sub>SiB<sub>2</sub>, as shown in Fig. 34) was annealed in a diffusion-pumped vacuum at 1600°C for a total of 120 hours. This resulted in removal of Si and the concomitant formation of a Mo-rich layer on the powder particles. The volume fraction of the Mo phase was not measured, but previous experience would indicate that it was on the order of 20 to 30 percent. In previous work, consolidation was achieved by hot isostatic pressing of such powders sealed in Nb cans (Ref. 11). In order to obtain a close-to-final shape, hot-pressing in cylindrical graphite dies was explored in the present work. The powder was hot-pressed in a graphite die in vacuum for 4 hr at 2073 K at an applied stress of 28 MPa. The final cylinder had a length of 32 mm and a diameter of 25 mm. According to metallographic examination, the pore volume fraction was 20 percent. In spite of this relatively high volume fraction, the porosity appeared to be discontinuous, since immersion of the hot-pressed piece in water or ethanol did not result in the formation of bubbles. This suggests that further consolidation to full density might be obtained by isostatic pressing at much higher pressures than can be achieved in a graphite hot press.



Since the results of the hot-pressing were encouraging, consolidation by hot-pressing at a somewhat higher temperature was examined. Powder with the composition Mo-16.8Si-8.4B (at. %) and a particle size ranging between 63 $\mu$ m and 250  $\mu$ m was subjected to several vacuum anneals in order to enrich the powder surfaces with Mo (by removing Si). The powder was consolidated into the form of a cylinder by hot-pressing for 4 hr at 2123 K and an axial stress of 35 MPa. Since a reaction zone with a thickness of about 0.5 mm formed between the powder and the die, it was difficult to remove the hot-pressed specimen after the run. Both the die and the specimen broke while attempting to release the 93-mm-long specimen. Figure 34 is an optical micrograph of a transverse section through one end of the consolidated cylinder. The bright phase is the Mo solid solution phase. It forms a continuous “binder” for large (100- $\mu$ m) Mo-Si-B grains. These grains in turn consist of a matrix of Mo<sub>3</sub>Si and Mo<sub>5</sub>SiB<sub>2</sub> containing small particles of Mo solid solution. The dark areas represent residual pores. These pores are evacuated since the hot-pressing was carried out in vacuum. It is anticipated that they can be removed by subsequent hot isostatic pressing at high pressures (e.g., 200 MPa) and high temperatures (e.g., 2000 K). Because of the continuous Mo matrix, the microstructure in Fig. 34 is expected to result in higher fracture toughness and ductility than the microstructure in Fig. 33.



Note: The volume fraction of the Mo solid solution phase is approximately 28 percent.

**Figure 34. Optical Micrograph of a Transverse Section of Vacuum-Annealed and Hot-Pressed Mo-16.8Si-8.4B (at. %) Powder**

#### 4.2.4 Thermal Shock

Thermal shock resistance is a serious problem with nozzle materials since large heat loads during facility startup may cause severe thermal gradients in the nozzle wall.. Quenching experiments were carried out in order to assess the thermal shock resistance

qualitatively. For comparison, a range of materials including the C103 (Nb-10 wt% Hf) alloy used for the T9 tunnel nozzle throat was examined (see Table 4).

**Table 4. Specimens Subjected to Thermal Shock Tests  
(Quenching from 1700 K into Water)**

Spec. No.	Composition	Diam. (mm)	Length (mm)	Mass (g)
N013	Nb-10 wt% Hf ("C-103")	20.2	12.6	35.7
N018	Mo <sub>3</sub> Si/Mo <sub>5</sub> SiB <sub>2</sub> intermetallic particles (Mo-20Si-10B, at. %), initial size 90-180 $\mu$ m, with nominally 17 vol% Mo on surface, hot-pressed in vacuum for 4 hr at 2073 K and 28 MPa	24.4	19.1	115.0
N019	Mo-8Si-11.2B, at. %, drop-cast in argon, isostatically hot-pressed for 4 hr at 1973 K and 210 MPa	18.7	26	72.4
N020	Mo-16.8Si-8.4B (at. %) powder, initial size 63-250 $\mu$ m, with nominally 28 vol. % Mo coating, hot-pressed in vacuum for 4 hr at 2123 K and 35 MPa	20.1	29.5	76.4
N011	Pure Mo, 25 by 12 by 6 mm			20.5
N012	TZM (Mo-0.5Ti-0.1Zr, wt%)	19	18	54.9

The specimens were encapsulated in quartz tubes that were first evacuated and then back-filled with argon to a pressure of 16 kPa. This pressure was chosen to provide 1 atm of pressure at 1700 K to prevent collapse of the tubes during annealing. After the loaded quartz tubes had been inserted into a furnace at 1700 K for 10 min, they were pulled out, inserted in water, and immediately broken. None of the specimens disintegrated. However, specimen N018 showed macrocracks traversing the whole diameter of the specimen. Metallographic examination showed that specimens N019 and N020 both contained radial macrocracks with typical lengths of 5 to 10 mm. Each of these specimens contained 14 such cracks around its cylindrical perimeter. Pure molybdenum (specimen N011) contained cracks that were more numerous, but were only 10 to 20  $\mu$ m long. TZM (specimen N012) did not show any cracks, and neither did the C103 alloy (specimen N013).

In thermal shock theory, one distinguishes between mild and severe thermal shock (Ref. 12). Whether a thermal shock is mild or severe depends on the Biot number,  $\beta$ :

$$\beta = t h/k$$

where  $t$  = thickness = 10 mm

$h$  = heat-transfer coefficient  $\approx 250,000 \text{ W/m}^2$  (for the A2Lite)

$k$  = thermal conductivity =  $138 \text{ W/(m}\cdot\text{K)}$  (for Mo at room temperature)

Mild thermal shock occurs for  $\beta \ll 2$ , whereas severe thermal shock occurs for  $\beta \gg 2$ . Assuming a molybdenum nozzle for the moment, the Biot number is 18 (i.e., the thermal shock is severe).

If inelastic deformation does not occur, the thermal contraction  $\varepsilon_t$  in severe thermal shock is instantaneously compensated by an elastic strain  $\varepsilon_e$ :

$$\varepsilon_t + \varepsilon_e = 0$$

where

$$\varepsilon_t = \alpha \Delta T$$

and

$$\varepsilon_e = \sigma(1-\nu)/E$$

Hereby  $\alpha$  is the thermal expansion of the Mo,  $\Delta T$  is the temperature change (negative for a temperature decrease),  $\sigma$  is the stress,  $\nu$  is Poisson's ratio, and  $E$  is Young's modulus. The factor  $(1-\nu)$  arises from the biaxiality of the stress state. The immediate result is:

$$\Delta T = -\sigma(1-\nu)/(\alpha E)$$

For a plastic material, the maximum instantaneous temperature change  $\Delta T$  for which plastic deformation is negligible occurs when the thermal stress reaches the yield stress, i.e., when  $\sigma = \sigma_y$ . For Mo near room temperature, the values are:

Yield Stress (20°C)	600 MPa
Young's modulus	329 GPa
CTE, 300 to 1700 K	6.4 ppm/K
Poisson's Ratio	0.31

Using these values we find  $\Delta T = -197 \text{ K}$ . This means that for a sudden temperature decrease greater than 197 K, plastic deformation must occur or else the Mo will crack. Because of its high strength, Mo-10Si-14B (at. %) can potentially withstand larger temperature decreases. For a yield strength of 2790 MPa, and with the other parameters being similar to those of Mo, the result is  $\Delta T = -918 \text{ K}$ . Since the brittle phases  $\text{Mo}_3\text{Si}$  and  $\text{Mo}_5\text{SiB}_2$  are flaw-sensitive, particularly in tension, it is unlikely that such high  $\Delta T$  values can be obtained in practice. If a continuous Mo phase is employed, its yield strength is relatively low, and plastic deformation will occur during severe thermal shock in which the temperature drops by more than a few hundred K. This discussion makes it clear that the thermal shock requirements for Mo-Si-B alloys can be satisfied only if the nozzle throat is preheated.

### 4.3 Mo-Re-X ALLOY DEVELOPMENT

Because of the thermal shock issue, Mo-Si-B alloys may have limited utility for hypersonic nozzles. If extremely high strength at very high temperatures is required, the Mo-Si-B alloys may be of interest as long as the thermal shock is minimized by the engineering design. However, more realistic, nearer-term materials systems that might, for example, be used in Tunnel 9 include Mo-Re alloys (Ref. 13), which are much more ductile than dilute Mo alloys such as TZM. The potential for strengthening Mo-Re with additional alloying elements is explored here.

#### 4.3.1 Mo-Re Alloy Baseline

Two 25-g buttons of Mo-Re-base alloys were cast and annealed for 1 hr at 1600°C in vacuum. In order to trap interstitial impurities such as C and O, a small amount of Zr was added in both cases. One button served as a ductile Mo-Re reference alloy, and in the other the Mo was partially substituted with 5 at. % Nb. The purpose of this experiment was to determine whether a) the Nb increases the strength and b) whether it reduces the room temperature ductility of Mo-Re. As a first step, the microhardness of the two alloys was measured. Although Nb has a significantly larger atomic size than Mo (1.44 vs. 1.37Å), it produces a relatively small hardness increase at room temperature.

**Table 5. Vickers Hardness (1000 g/ 15-s Dwell Time) of Mo-Re Alloys**

	Composition (at. %)	HV(1000g)	Std Dev
N024-1	Mo-26Re-0.1Zr	285	12
N025-1	Mo-5Nb-26Re-0.1Zr	318	9

Miniature bend bars with a cross section of 2 by 2 mm and a length of approximately 12 mm were EDM'd from Mo-26Re-0.1Zr (alloy N024) and Mo-5Nb-26Re-0.1Zr (alloy N025). After being ground with 180-grit SiC paper, the bend bars were tested by three-point bending at room temperature. Mo-26Re-0.1Zr was clearly ductile. Mo-5Nb-26Re-0.1Zr was not entirely brittle, but broke by controlled crack propagation instead. Mo-26Re-0.1Zr had a grain size on the order of 0.3 mm and, at variance with published data, exhibited no crystallographic twinning in the deformation zone. Mo-5Nb-26Re-0.1Zr, on the other hand, had a grain size of less than 0.2 mm and showed profuse twinning in its deformation zone.

It is difficult to assess ductility by bend testing; tensile tests provide not only a quantitative value for the ductility, but also a value for the yield stress. Miniature tensile specimens with a thickness of 0.6 mm, an overall length of 16 mm, and a gage length of 5 mm were machined by EDM out of the Mo-26Re-0.1Zr button and have been tested at room temperature.

#### 4.3.2 High-Strength Mo-Re-X Alloy Development

The alloy-development approach followed here was as follows: materials with alloying additions that do not degrade the room-temperature ductility will be compression

tested at 1427°C in order to determine whether these alloying additions improve high-temperature strength.

#### 4.3.2.1 Strength at Room Temperature

In addition to the existing compositions Mo-26Re-0.1Zr and Mo-5Nb-26Re-0.1Zr (at. %), two more buttons with compositions Mo-26Re and Mo-26Re-0.3Zr (at. %) were prepared by arc-casting. The compositions of the latter two buttons were chosen in order to assess the influence of Zr on the ductility of Mo-26Re. Whereas conventional Mo alloys typically contain Zr as an oxygen getter and carbide former, the effect of Zr on the ductility of Mo-Re alloys does not appear to have been examined to date.

All buttons were annealed for 1 hr at 1600°C in vacuum. Miniature tensile test specimens (thickness 0.6 mm, gage length 5 mm) were electrodischarge-machined from the annealed buttons. Table 6 shows the 0.2-percent yield stress (YS), the ultimate tensile stress (UTS), and the ductility obtained in the room-temperature tensile tests. The results indicate that an addition of 0.1 at. % Zr is beneficial for the room-temperature ductility. The effect of Zr on the yield strength of Mo-26Re is not known, since 0.2-percent yield stress data could not be obtained for the alloys with 0 and 0.3 at. % Zr. Both these alloys broke, or showed sudden load drops, before reaching a plastic elongation of 0.2 percent. However, atomic size consideration suggests that Zr, which is a larger atom than Mo or Re, will provide significant solid solution strengthening ( $r_{\text{Mo}} = 1.37 \text{ \AA}$ ,  $r_{\text{Re}} = 1.34 \text{ \AA}$ ,  $r_{\text{Zr}} = 1.57 \text{ \AA}$ ). The Zr concentration that provides the highest ductility is not presently known, but it appears to be  $> 0$  and  $< 0.3 \text{ wt\%}$ .

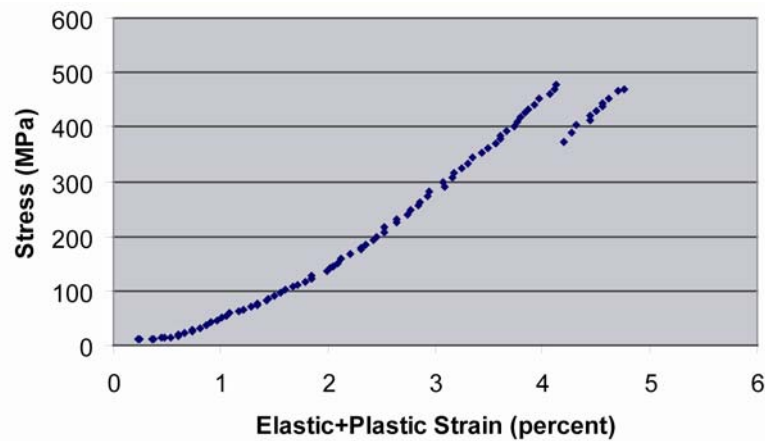
Previously the effects of Zr additions of 0, 0.1, and 0.3 at. % on the ductility of Mo-26 at. % Re were examined. In order to more accurately determine the Zr concentration producing in the maximum room-temperature ductility, a Mo-Re specimen containing 0.05 at. % Zr was prepared. Its tensile properties are shown in Table 7 (N031).

The measured stress-strain curves for the miniature test specimens showed frequently sudden load drops, which are attributed to sudden crack propagation in the gage length. Sometimes several load drops were observed until final fracture occurred. Figure 35 shows an example of a stress-strain curve. Table 6 documents the load drops in more detail. Also, two new alloys, Mo-26Re-1Al and Mo-26Re-1Al-0.1Zr, at. %, have been added. Even though only 1 at. % Al has been added, the room-temperature ductility is seriously degraded. However, one of the Mo-26Re-1Al-0.1 Zr specimens did show a small amount of ductility, indicating that Zr has a beneficial effect also in Al-containing alloys.

**Table 6. Room-Temperature Tensile Test Data for Mo-26Re (at. %) Alloys\***

	Composition (at. %)	0.2% YS (MPa)	UTS (MPa)	Plastic Strain at First Load Drop (%)	Final Strain to Fracture	No. of Load Drops
N026-T1	Mo-26Re		452	0	0	1
N026-T2	"	>477	477	0	0.6	2
N031-T1	Mo-26Re-0.05Zr	>343	343	0	0	1
N031-T2	"	>355	355	0	0	1
N024-T1	Mo-26Re-0.1Zr	596	644	1.2	6.2	2
N024-T2	"	635	720	10.6	10.6	1
N027-T1	Mo-26Re-0.3Zr	>347	347	0	0	1
N027-T2	"	>473	473	0	0	1
N028-T1	Mo-26Re-1Al	>424	424	0	2.2	2
N028-T2	"	>343	343	0	0	1
N29-T1	Mo-26Re-1Al-0.1Zr	>631	631	0	7.1	3
N29-T2	"	654	656	0.3	2	2
N30-T1	Mo-26Re-5Ti-0.1Zr	>190	190	0	0	1
N30-T2	"	>385	385	0	0	1
N032-T1	Mo-26Re-5Ta-0.1Zr	>396	396	0	0	1
N032-T2	"	>337	337	0	0	1
N033-T1	Mo-26.7Re-7.6Cr-0.1Zr	>441	496	0	2.2	2
N033-T2	"	522	560	0.2	2	2

\* The arc-cast alloys were annealed for 1 h at 1600°C in vacuum except for the Mo-Re-Cr-Zr alloy (N033), which was annealed for 1 hr at 1400°C.

**Figure 35. Room-Temperature Tensile Test of Mo-26 at. % Re (Test N026-T2)**

It should be pointed out that a small degree of ductility in the miniature specimens will probably translate into much higher ductility values for larger specimens made from more elaborately processed material. This is because the miniature specimens are fabricated from large-grained cast and annealed materials. They have not been thermomechanically processed in order to reduce their grain size and improve their

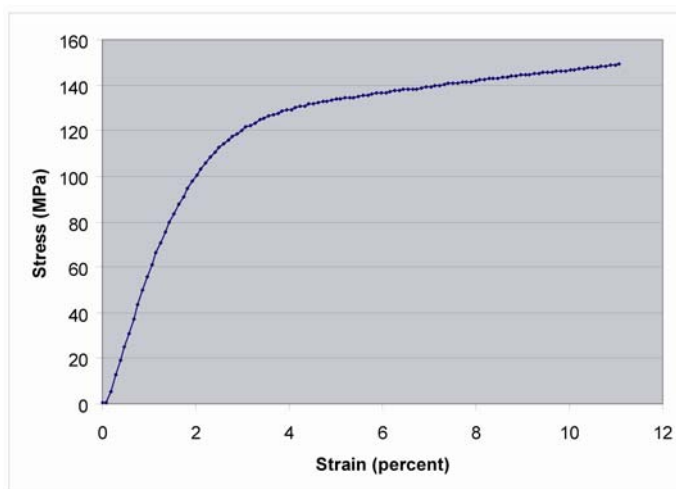
homogeneity. Also, the gage length of the miniature specimens was finished only with 325-grit SiC paper; a better finish might improve the ductility.

Table 6 includes several additional alloys. Microalloying of Mo-26 at. % Re with different concentrations of Zr showed that adequate room temperature ductility was observed for 0.1 at. % Zr. An addition of 5 at. % Ti embrittled the materials since fracture occurred at relatively low stresses. Alloying with 7.6 at. % Cr, on the other hand, was not as detrimental, since some ductility was maintained. Surprisingly, the yield stress of Mo-26.7Re-7.6Cr-0.1Zr is less than that of Mo-26Re-0.1Zr. It has not yet been determined whether Cr additions to Mo-26 at. % Re actually cause solid solution softening, or whether the strength difference is caused by differences in the grain size. It has also not yet been determined to what extent solid solution alloying additions such as Al, Ti, or Cr improve high-temperature strength (which is the goal of this research). It should be noted that the changes in the high-temperature strength attributable to Al, Ti, or Cr may be quite different from those observed at room temperature.

Table 6 also includes a Ta-containing alloy (N32). Similar to Ti, Ta additions degrade the room temperature tensile ductility of Mo-Re alloys.

#### 4.3.2.2 Strength at High Temperature

For the high-temperature testing, a calibration curve of the furnace setting required to reach a particular temperature at a thermocouple embedded in a dummy specimen was obtained. Subsequently, high-temperature compression tests of Mo-Re-X alloys were carried out in argon at a temperature of 1427°C and a strain rate of  $10^{-3} \text{ s}^{-1}$ . Figure 36 shows a plot of the engineering stress vs. the engineering strain for Mo-26Re-0.05Zr (at. %). Its 0.2-percent yield stress was 94 MPa (see Table 7). For comparison, Mo-26Re-5Nb-0.1Zr (at. %) tested under the same conditions showed a yield stress of 156 MPa. The niobium solid solution addition thus caused a significant improvement of the high-temperature strength.



**Figure 36. Stress-Strain Curve for Compression of Mo-26Re-0.05Zr (at. %) at 1427°C and  $10^{-3} \text{ s}^{-1}$**

**Table 7. 0.2-Percent Yield Stress Values at 1427°C and a Strain Rate of  $10^{-3} \text{ s}^{-1}$**

N031-C2	Mo-26Re-0.05Zr	94
N025-C1	Mo-26Re-5Nb-0.1Zr	156
N033-C1	Mo-26.7Re-7.6Cr-0.1Zr	192

Table 7 shows the results of high-temperature compression data discussed previously, as well as results for Mo-Re-Cr-Zr. Chromium additions cause pronounced high-temperature strengthening. Since tensile tests with Cr-containing alloys suggest limited ductility (see Table 6), Cr additions are of particular interest in the development of high-strength Mo-Re alloys.

#### 4.3.3 Oxygen Embrittlement

The residual oxygen and carbon concentration of Mo-26 at. % Re (specimen N026) was determined (see Table 8). The oxygen concentration is relatively high. For a Zr concentration of 0.05 at. %, all the oxygen can in principle be tied up by the formation of  $\text{ZrO}_2$ . However, it appears that more Zr than that is required, since adequate room-temperature ductility required an addition of 0.1 at. % Zr.

**Table 8. Carbon and Oxygen Concentrations in Mo-26 at. % Re (Specimen N026)**

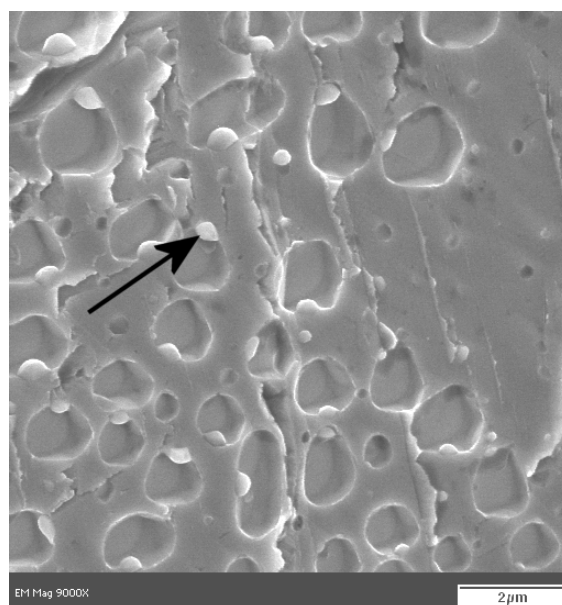
	wppm	appm	at. %
carbon	70	600	0.06
oxygen	160	1000	0.1

In pure Mo or dilute Mo alloys, the high oxygen concentration listed in Table 8 would most definitely result in intergranular fracture at room temperature. However, the fracture in Mo-26 at. % Re was transgranular, albeit brittle. (Previously conducted room-temperature tests showed zero tensile ductility for Mo-26 at. % Re.) Consistent with the high oxygen concentration, small, oxygen-containing nodules were found on a room-temperature fracture surface (Fig. 37). Because of the small size of the nodules, a precise chemical analysis could not be carried out. However, energy-dispersive spectroscopy (EDS) in a scanning electron microscope (SEM) indicated a composition near  $\text{MoO}_2$ , with a small amount of Re. Mo-26Re-0.1Zr (at. %), in contrast, exhibited strains to fracture of several percent. It is therefore concluded that the residual oxygen in Mo-26 at. % Re resulted in (transgranular) embrittlement, and that Zr additions were effective in gettering the residual oxygen, thus improving ductility. The Zr did not change the fracture mode, which remained cleavage.

#### 4.3.4 Compression Testing

Because of premature fracture, the room temperature yield strength of several ternary Mo-Re-X alloys could not be determined in tension. Compression specimens





Note: Arrow indicates typical nodule.

**Figure 37. Oxygen-Containing Nodules on a Room-Temperature Fracture Surface of Mo-26 at. % Re**

were fabricated and tested at a strain rate of  $1 \times 10^{-3} \text{ s}^{-1}$ . Even though the tests were carried out in compression, some of the specimens showed sudden load drops. If a load drop occurred prior to reaching the 0.2-percent yield stress, it was taken to be the lower limit of the yield stress. The results of the compression tests, which include the previously obtained results for specimens N033-C2 and N033-C3, are listed in Table 9.

**Table 9. Results of Room Temperature Compression Tests.**

Spec No.	Comp (at. %)	0.2% yield stress (Mpa)	Results
N027-C1	Mo-26Re-0.3Zr	550	
N030-C1	Mo-26Re-5Ti-0.1Zr	643	
N032-C1	Mo-26Re-5Ta-0.1Zr	>660	Load drop prior to yield
N034-C1	Mo-26Re-5Hf-0.1Zr	780	
N035-C1	Mo-26Re-5Hf-0.1Zr-1C	>790	Load capacity of equipment reached
N033-C2	Mo-26.7Re-7.6Cr-0.1Zr	>422	Load drops prior to yield
N033-C3	"	>467	Load drops prior to yield

Table 9 shows that Ti, Ta, Hf, and Hf+C additions cause pronounced strengthening at room temperature. While some of these alloys were previously shown to be brittle in tension at room temperature, it should be considered that they have not been thermomechanically processed to homogenize them and to reduce their grain size. A recent publication suggests that the room temperature ductility of thermomechanically processed Mo-Re-X alloys containing > 5 at. % of Ti, Ta, and Nb is 20 percent or above. (See: K. B. Povaraova and M. A. Tylkina, "Physicochemical Principles of the Design of Rhenium Alloys," in "Rhenium and Rhenium Alloys," B. D. Bryskin, ed., TMS, 1997, pp. 647-659.)

### 4.3.5 Fracture Surface Analysis

The room-temperature fracture surfaces of two Mo-Re alloys were examined. Figure 38 shows a scanning electron micrograph (SEM) of Mo-26Re-0.1Zr (at. %). As noted previously, fracture is transgranular even though the grain size is large (several hundred micrometers). The fracture surface of Mo-26.7Re-7.6Cr-0.1Zr (at. %) is also transgranular (Fig. 39). It is concluded that the alloying element Cr does not change the typical fracture mode of Mo-26 at. % Re alloys and that Cr does not reduce the grain boundary strength of Mo-Re.

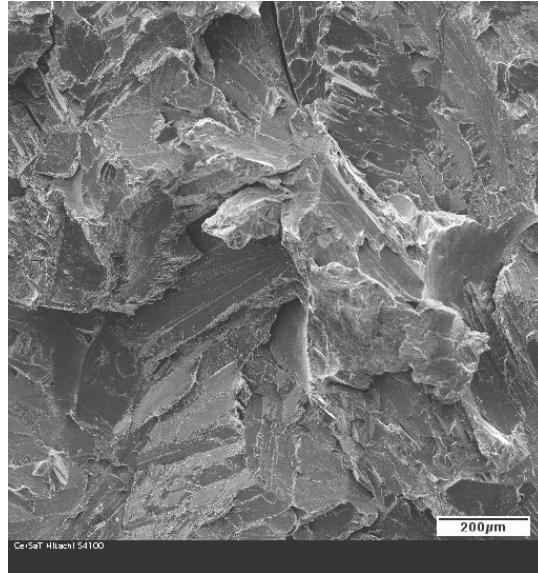


**Fig. 38 Room Temperature Fracture Surface of Mo-26Re-0.1Zr (at. %)**

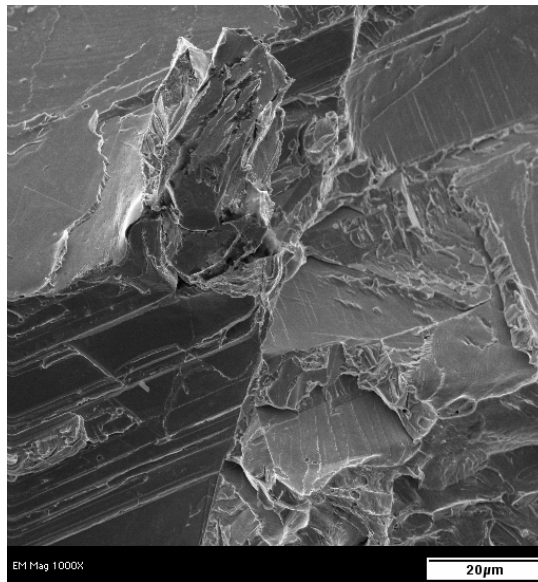


**Figure 39. Room Temperature Fracture Surface of Mo-26.7Re-7.6Cr-0.1Zr (at. %)**

#### 4.4 Ni-COATED Cu - BACKSIDE-COOLED ARC-HEATER NOZZLES

Early work by F. Shope (1994 memo and Ref. 5) showed that thermal barrier coatings on the inside of copper-base, backside-cooled arc-heater nozzles can improve performance. In particular, they allow higher operating pressures. Shope's work focused on ceramic coatings, which are brittle. In the present work, metallic Ni-based layers are being explored. Although they do not have the temperature capability of ceramics such as  $\text{ZrO}_2$ , they still have a significantly higher melting point than copper, and their thermal conductivity is also significantly lower than that of copper. Below is a compilation of relevant data. If the calculations based on those data show that Ni-based coatings or clads are advantageous, preliminary experimental work on the fabrication and integrity will be carried out.

**Table 10. Strength of Hot-Rolled Inconel 600 (Ni-16Cr-6Fe, wt%)**

T, °C	0.2% Yield Stress (MPa)	Ultimate Tensile Stress (MPa)
20	250	590
400	185	560
600	150	530
800	95	250
1000		110

**Table 11. Physical Properties of Inconel 600**

Specific gravity	8.42 g/cm <sup>3</sup>
Specific heat	0.46 J/(g K)
Thermal conductivity	14.8 W/(m K)

**Table 12. Thermal Expansion of Copper and Nickel, Percent**

T, °C	Cu	Ni
20	0.000	0.000
127	0.182	0.150
227	0.362	0.300
327	0.549	0.460
427	0.741	0.620
477	0.840	0.700
527	0.939	0.780
627	1.147	0.950
727	1.366	1.130
927	1.838	1.480

#### Data Sources:

*Smithells Metals Reference Book*, 8th edition, W. F. Gale and T. C. Totemeier, eds., Elsevier, New York, 2004.

*Thermophysical Properties of Matter*, Y. S. Touloukian, ed., Vol. 12, Part 1, 1975.

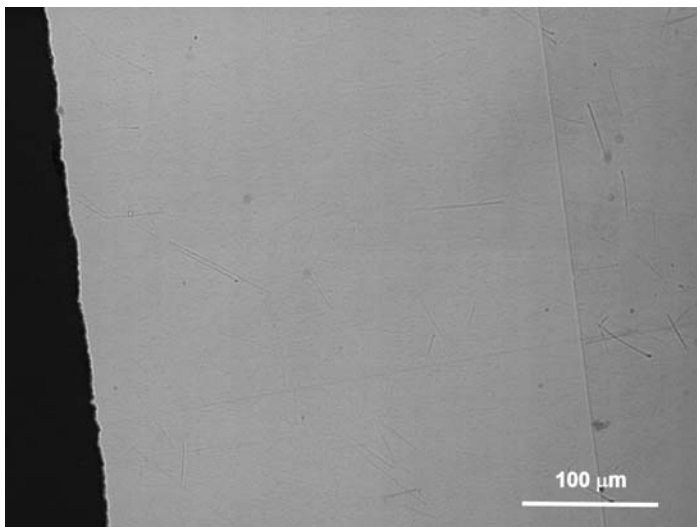
Calculations carried out by Fred Shope at AEDC showed that a 0.5-mm-thick nickel coating on the interior of a copper arc nozzle with a wall thickness of 1.65 mm improved nozzle performance (see Fig. 11). A major reason for this is the higher temperature capability of Ni as compared to that of Cu. The predicted performance improvement was not as pronounced as that afforded by a zirconia coating. However, zirconia has a much lower coefficient of thermal expansion than Cu (approximately 9 ppm/K vs. 18 ppm/K), and it is brittle. Therefore a zirconia coating is likely to crack during service. An Ni or Ni-based coating, on the other hand, is similar to Cu in its thermal expansion, and it is ductile. An Ni-based coating is therefore more likely to survive the operating conditions than a zirconia coating.

Because of the geometry of the copper arc nozzles, and because arc nozzles rely on work hardening for strengthening, high-temperature processes for applying an internal coating do not appear to be a good option. Electroplating may be the best way to apply the internal coatings. A vendor for electroplating Ni at minimal cost has been identified: Technic Inc ([www.technic.com](http://www.technic.com)). Solid solution Ni alloys are preferred to pure Ni because of a) their higher strength and b) their lower thermal conductivity, which allows the use of thinner coatings. Technic does not appear to routinely electroplate Ni alloys. According to the Metals Handbook (ASM, Vol. 5, 1994), electroplating with Ni-Fe and Ni-Co is possible, but no vendor has been identified so far. A group headed by Christopher A. Schuh at MIT is experienced in electroplating nanocrystalline Ni-W alloys. Thus it appears that there are several options for electroplating Ni-based alloys.

A piece of the Amzirc copper-base material from which the AEDC arc-heater nozzles are fabricated was received from AEDC. Slices of Amzirc copper-base material with a thickness of 1.5 mm have been electrodischarge machined. R. C. Waldrop from the Y-12 facility near ORNL was selected to provide initial Ni-plating experiments since he has many years of experience with electroplating. Tensile specimens were machined so that they could be tested in order to obtain information on the ductility and adherence of the Ni coating. The Ni-plating of the Amzirc copper sheets (thickness approx. 1 mm) was carried out as follows:

- (1) Abrade with 600-grit SiC paper to remove electrodischarge machining damage, and remove sharp edges
- (2) Scrub with abrasive cleaner
- (3) Rinse
- (4) Scrub with 409 cleaner
- (5) Rinse
- (6) Pickle in 35-percent sulfuric acid
- (7) Immerse in plating bath without rinsing, with current of 20 amps per sq ft
- (8) Electroplate for 24 hr in nickel sulfamate, 10 oz per gallon of water, pH 4.5 at 120°F

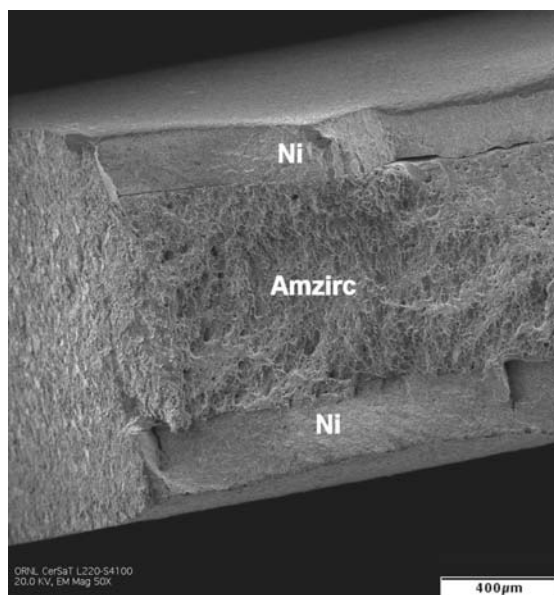
The thickness of the Ni coating varied between 0.2 and 0.4 mm. Figure 40 shows a cross section through the coated material. A tensile specimen with a gage length of 12.7 mm was electrodischarge machined from the plated material and tested at a strain rate of  $2 \times 10^{-3} \text{ s}^{-1}$  at room temperature. The elongation to fracture was determined to be 7.2 percent, and the ultimate tensile strength was 572 MPa. Currently, the surface of the gage section and the fracture surface are being examined in order to examine the integrity of the coating.



**\*Note:** The nickel coating, which has a thickness of approx. 0.4mm, is on the left-hand side of the micrograph.

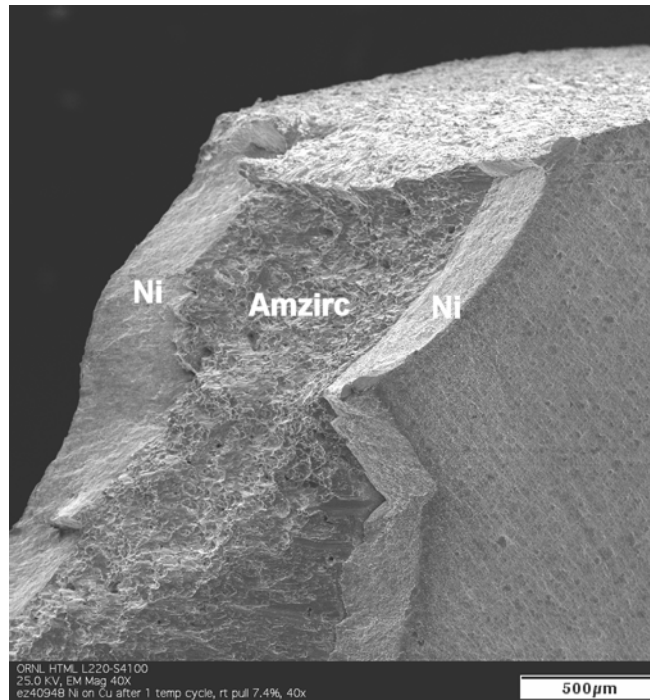
**Figure 40. Optical Micrograph of Cross Section Through Electroplated Amzirc Material.**

Figure 41 shows the room temperature fracture surface of an Amzirc copper alloy coated with Ni, without any additional heat treatment. The ductility of this specimen was 7.2 percent. Delamination between the Ni layers on top and bottom is observed, indicating inadequate bonding.



**Figure 41. SEM Micrograph of Room-Temperature Fracture Surface of As-Plated Amzirc.**

A Ni-coated Amzirc specimen was vacuum-annealed for 30 min at 800°C. The annealing decreased the ultimate tensile strength from 572 to 283 MPa. At the same time, the elongation to fracture increased from 7.2 to 38.5 percent. An SEM micrograph of this specimen is shown in Fig. 42. Examination at higher magnifications did not show any evidence of delamination. This is attributed to the significantly lower flow stresses, as compared to the as-plated material. Also, the annealing must have resulted in interdiffusion between the Cu and the Ni. (Cu and Ni form a continuous solid solution.) The interdiffusion is likely to strengthen the interfacial bonding.



**Figure 42. SEM of Fracture Surface of Ni-Plated and Annealed Amzirc Sheet**

## 5.0 SUMMARY/CONCLUSIONS

Advances have been made in the development of new materials suitable for various hypersonic nozzle applications. Nozzle survivability requirements for various nozzles were reviewed. Advances in the development of suitable nozzle materials are as follows:

- 1) The Iridium alloy (Ir-Zr) is especially applicable to moderate recovery-temperature, heat-sink nozzle applications such as RDHWT. The basic strength requirements at high temperature (600 MPa at 1700 K) are satisfied. However, a more detailed analysis including pressure and thermal stresses (See Section 4.1.5) indicates that some surface damage is to be expected, thus limiting the lifetime of the nozzle. Oxidation resistance appears to be good. An ingot large enough to supply material for three A2Lite nozzles has been successfully fabricated. One A2Lite nozzle has been machined and is available for future A2Lite nozzle testing.

- 2) Mo-Si-B alloys have been developed with sufficient strength at elevated temperatures for either the RDHWT or AEDC Tunnel 9 applications. However, their lack of oxidation resistance and vulnerability to thermal shock limits their utility.
- 3) Mo-Re-X alloys show promise for strength at elevated temperature applications.
- 4) Initial investigations of Ni-coated Cu show promise for backside-cooled nozzle applications.

The information documented here has also been disseminated in part in Refs. 14 through 18.

### **Acronyms**

AEDC	Arnold Engineering Development Center
APTU	AEDC Aerodynamic and Propulsion Test Unit
DPH	Diamond pyramid hardness
EDM	Electrodischarge machining
EOS	Equation of state
FEA	Finite-element analysis
FPST	Free-piston shock tunnel
MHD	Magnetohydrodynamic
MTS	Material Testing System
NIST	National Institute of Standards and Technology
ORNL	Oak Ridge National Laboratories
RDHWT	Radiatively Driven Hypersonic Wind Tunnel
RLV	Reusable launch vehicle
RV	Reentry vehicle
SEM	Scanning electron microscope

## **6.0 REFERENCES**

1. Best, J. T., Tirres, C., Fetterhoff, T., Crook, R. T., Laster, L., and Jordan, J. "RDHWT/MARIAH II Hypersonic Wind Tunnel Program Overview and Requirements." AIAA Paper 2000-2273, Denver, CO, June 19-22, 2000.
2. Costantino, Marc, Brown, G., Raman, K., Miles, R., and Felderman, J. "Ultra-High Pressure Driver and Nozzle Survivability in the RDHWT/MARIAH II Hypersonic Wind Tunnel." AIAA Paper 2000-2275, Denver, CO, June 19-22, 2000.

3. Brown, G. L., Girgis, I. G., and Miles, R. B. "Predictions for the Heat Transfer and Boundary Layer Growth in the Radiatively Driven Hypersonic Wind Tunnel and Comparisons with Experiment at Ultra-high Reynolds Number" AIAA Paper 2002-3128, St. Louis, MO, June 24-26, 2002.
4. Enkenhus, K. R., and Maher, E. F. "The Aerodynamic Design of Axisymmetric Nozzles for High-Temperature Air" NAVWEPS Report 7395, February 1962.
5. Shope, F. L., "Conceptual Thermal Design of a Backside Cooled Throat for an Aeropropulsion Test Facility." AIAA-2001-0612, AIAA 39th Aerospace Sciences Meeting and Exhibit, Reno, NV, Jan. 8-11, 2001.
6. Nieh, T. G., Wang, J.G. and Liu, C. T. 2000. "Deformation of a Multiphase Mo-9.4Si-13.8B Alloy at Elevated Temperatures." *Intermetallics*, Vol.9, No.1, 2001 pp.73-79 .
7. George, E. P. and Liu, C. T. "Micro- and Macro-alloying of Ir-base Alloys." *Iridium*, ed. Ohriner, Lanam, Panfilov and Harada, TMS Publication, 2000, pp. 3-14.
8. Schneibel, J. H., Liu, C. T. and Carmichael, C. A. "Strength and Fracture Toughness of Cast Mo-12Si-8.5B (at. %) Intermetallics." Min. Met. Mater. Soc. Symp. on Structural Silicides, San Diego, CA USA, TMS, Feb. 28-Mar 4, 1999.
9. Schneibel, J. H., Kramer, M. J., Ünal, Ö, and Wright, R. N. (2001), "Processing and Mechanical Properties of a Molybdenum Silicide with the Composition Mo-12Si-8.5B (at. %)" *Intermetallics*, 9(1), 25-31.
10. Schneibel, J. H., "High Temperature Strength of Mo-Mo<sub>3</sub>Si-Mo<sub>5</sub>SiB<sub>2</sub> Molybdenum Silicides." *Intermetallics* 11[7] (2003) 625-632.
11. Schneibel, J. H., Kramer, M. J., Easton, D. S. "A Mo-Si-B Intermetallic Alloy with a Continuous  $\alpha$ -Mo Matrix" *Scripta Materialia* 46 (3) (2002) pp. 217-221.
12. Pickles, C. S. J. and Field, J. E. "The Laboratory Simulation of Thermal Shock Failure." *J. Phys. D: Appl. Phys.* 29 [2] (1996) 436-441.
13. Agnew, S. R. and Leonhardt, T., "The Low-Temperature Mechanical Behavior of Molybdenum-Rhenium" *JOM*, October 2003, pp. 25-30.
14. Felderman, E. J., Shope, F. L., Liu, C. T., and Schneibel, J. "Potential New Materials for Hypersonic Nozzles" 2003 National Space and Missile Materials Symposium (NSMMS), San Diego, CA, June 23-26, 2003.
15. Felderman, E. J., Shope, F. L., and Akers, D.T. "Energy Management for Hypersonic Heat-Sink Nozzles" 12th AIAA International Space Planes and Hypersonics Systems Technologies Conference, AIAA-2003-7002, Norfolk, VA. December 15-19, 2003.



16. Felderman, E. J., Shope, F. L., Liu, C. T., Easton, D. S. and Schneibel, J. "Development & Testing of New Materials for Hypersonic Nozzles," 2004 ITEA (International Test and Evaluation) Technology Review, June 7-10, 2004, Monterey, CA
17. Schneibel, J. H. and Felderman, E. J. "Development and Testing of New Materials for Aerospace Applications" AIAA Paper 2004-2593, June 2004.
18. Felderman, E. J. and Schneibel, J. H. "Development of an Iridium Alloy for Hypersonic Nozzles" 2005 ITEA (International Test and Evaluation) Technology Review, July 12-14, 2005, Atlanta, GA